CERN-LPCC-2017-XX

Dark Matter Working Group recommendation for Two Higgs Doublet Model (draft title)

Authorlist to be compiled; Antonio Boveia,[3,*] Caterina Doglioni,[8,*] Kristian Hahn,[14,*] Ulrich Haisch,[15,16,*] Steven Lowette,[22] Tim M.P. Tait,[25,*]

[*]DMWG organizers

[3]Ohio State University, 191 W. Woodruff Avenue Columbus, OH 43210

[8]Fysiska institutionen, Lunds universitet, Lund, Sweden

[14]Department of Physics and Astronomy, Northwestern University, Evanston, Illinois 60208, USA

[15]Rudolf Peierls Centre for Theoretical Physics, University of Oxford, Oxford, OX1 3PN, United Kingdom

[16]CERN, TH Department, CH-1211 Geneva 23, Switzerland

[22]Physics Department, Vrije Universieit Brussel, Brussels, Belgium

[25]Department of Physics and Astronomy, University of California, Irvine, California 92697, USA

Editor's E-mail: antonio.boveia@cern.ch, caterina.doglioni@cern.ch, kristian.hahn@cern.ch, ulrich.haisch@physics.ox.ac.uk, ttait@uci.edu

Abstract. Draft abstract.

Contents

1 Introduction

Reasoning behind this effort

- Simplified models only one signature at a time, sometimes not gauge invariant
- One step beyond this: less-simplified models
- Compare and confront different search sensitivity
- Combinations among different signatures
- Find new kinematic regimes / improve searches by exploring different signatures
- Still keeping the choice of model generic enough that this is reusable for theorists

Reasoning behind this effort

- Reasoning behind the choice of model
- Highlights more than one signature at a time, depending on parameters
- Leaves room for new unexplored kinematic signatures within existing searches (left for future work)
- Complete enough, still simplified so that one can choose grid planes
- Existing theory effort (HXSWG)

2 The model

Description of the model

- Citations: [1–5]
- Particles, masses, couplings, mixing angles

Comparison with existing models How does the model compare with other 2HDMs/scalar models (with and without DM).

- Scalar to SSM to 2HDM evolution
- Other models:
  - S. Ipek, D. McKeen, A. Nelson, [3]
  - Bell, Busoni, Sanderson, [2]
  - No, Goncalves, Machado, [4, 5]
  - Higgs Cross-section Working Group

3 Model parameters

- Motivate the choice of parameters in [1]
- Vacuum stability study: fix lambda parameters to 3

  For extension of the Higgs sector (and in general for scalar extensions of the Standard Model) one needs to worry about boundedness from below of the scalar potential, as well as absolute stability of the electroweak minimum[1].

[1] We remark here that implications from all indirect constraints - be it flavour, electroweak precision constraints or stability requirements - should be treated as preferred parameter space in a simplified model framework. It would contradict the idea of simplified models were these constraints taken at face value.

Regarding boundedness from below of the scalar potential in the present 2HDM + S model, we stress that provided that $\lambda_{P1},\, \lambda_{P2} > 0$ in

$$
\begin{aligned}
V_{\rm P} = \ & \frac{1}{2} m_P^2 P^2 + \kappa \, (i \, P \, H_1^\dagger H_2 + \text{h.c.}) \\
& + \lambda_{P1} \, P^2 \, |H_1|^2 + \lambda_{P2} \, P^2 \, |H_2|^2 \, ,
\end{aligned}
$$

the study of boundedness from below at tree-level reduces to the corresponding study in the 2HDM. The boundedness from below conditions in this case are well-known [6]:

$$
\lambda_1 > 0 \, , \quad \lambda_2 > 0 \, , \quad \lambda_3 > -\sqrt{\lambda_1 \lambda_2} \, , \quad \lambda_3 + \lambda_4 - |\lambda_5| > -\sqrt{\lambda_1 \lambda_2} \tag{3.1}
$$

and can be inferred from analyzing the scalar potential at large field values $H_1,\, H_2 \gg v$. For $m_{H^\pm} = m_{H_0}$, the first two conditions in (3.1) may be simply written as

$$
\frac{m_h^2}{v^2}(1 - t_\beta^2) + \lambda_3 \, t_\beta^2 > 0 \, , \qquad \frac{m_h^2}{v^2}(1 - t_\beta^{-2}) + \lambda_3 \, t_\beta^{-2} > 0 \tag{3.2}
$$

which result in the requirement $\lambda_3 > m_h^2/v^2 = 0.258$. In figure 1 we show the regions of parameter space in the $(m_a,\, m_{H_0})$ (left) and $(s_\theta,\, m_a)$ (right) planes for which the tree-level boundedness from below conditions 3.1 are satisfied, assuming $m_{H^\pm} = m_{H_0} = m_{A_0}$.

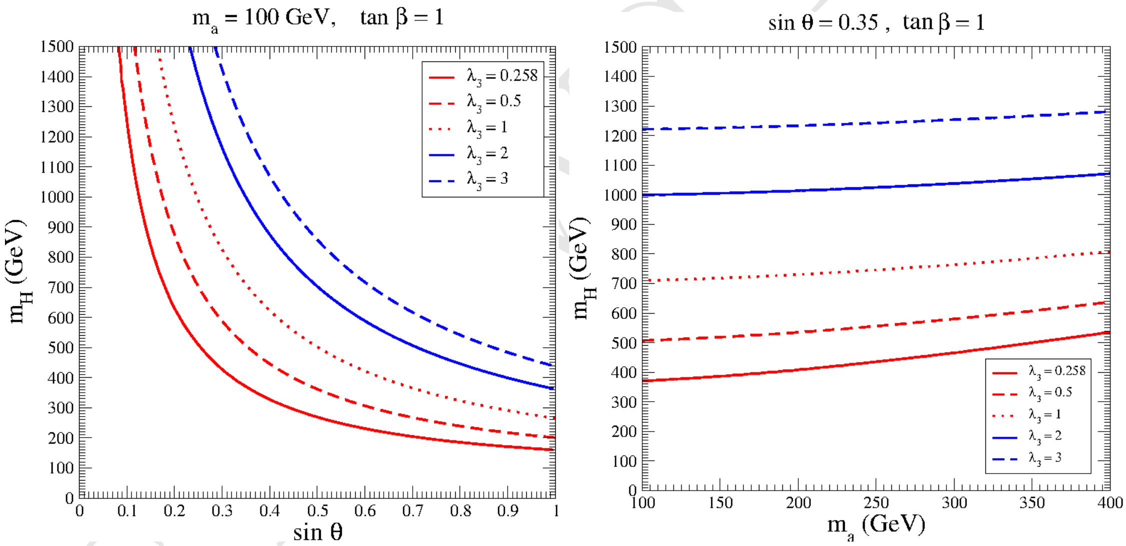

Figure 1: Regions of parameter space in the $(m_a,\, m_{H_0})$ (left) and $(s_\theta,\, m_a)$ (right) planes for which the tree-level boundedness from below conditions 3.1 are satisfied, assuming $m_{H^\pm} = m_{H_0} = m_{A_0}$.

Figure 1 shows that the region satisfying the tree-level boundedness from below conditions increases as λ_3 increases. At the same time, the choice $\lambda_3 = \lambda_{P1} = \lambda_{P2}$ which we adopt in the present analysis allows the increase in λ_3 not to affect the mono-Higgs sensitivity via a change in the coupling g_{aAh}

$$
\begin{aligned}
g_{aAh} &= \frac{c_\theta \, s_\theta}{m_H \, v} \left[m_h^2 + m_H^2 - m_a^2 - 2(\lambda_3 - \lambda_{P1} c_\beta^2 - \lambda_{P2} s_\beta^2) v^2 \right] \\
&= \frac{c_\theta \, s_\theta}{m_H \, v} \left[m_h^2 + m_H^2 - m_a^2 \right]
\end{aligned} \tag{3.3}
$$

We then fix the value $\lambda_3 = 3$ as benchmark for the rest of our analysis.

A few comments are in order.

- The choice of λ_3, motivated by boundedness from below conditions, while not affecting the mono-Higgs sensitivity if $\lambda_3 = \lambda_{P1} = \lambda_{P2}$, has an impact on the mono-Z sensitivity since the coupling

$$\begin{aligned} g_{Haa} &= \frac{1}{m_H\, v}\left[2\, t_{2\beta}^{-1}\, s_\theta^2\, (m_h^2 - \lambda_3 v^2) + s_{2\beta}\, c_\theta^2 v^2 (\lambda_{P1} - \lambda_{P2})\right] \\ &= \frac{1}{m_H\, v}\left[2\, t_{2\beta}^{-1}\, s_\theta^2\, (m_h^2 - \lambda_3 v^2)\right] \end{aligned} \tag{3.4}$$

  does depend on λ_3 and influences the balance between $\Gamma(H_0 \to aa)$ and $\Gamma(H_0 \to Za)$ which ultimately determines the $H_0 \to Za$ branching fraction. In short, the choice of λ_3, λ_{P1}, λ_{P2} affects either mono-Higgs or mono-Z sensitivities (or both).
- Together with boundedness from below, other potential constraints are usually considered in the context of the 2HDM and apply in general, among them unitarity (see e.g. [7, 8]) and absolute stability of the electroweak vacuum (see e.g. [9]). In the present context we find these constraints are generically weaker than the boundedness from below condition and therefore disregard them in the following.
- The boundedness from below conditions are here evaluated at tree-level, but in a fully consistent treatment they should be evaluated including the effect of radiative corrections. This is however a much more involved process than what has been discussed above for the tree-level case (see e.g. [10]). In addition, the boundedness from below constraints discussed here are potentially sensitive to the existence of UV physics which our 2HDM+S simplified does not capture, and which could modify the above picture through the presence of higher-dimensional operators. Still, it is worth pointing out that for the 2HDM+S simplified model to be a good description of LHC phenomenology we require the new physics scale suppressing these effective operators to be above the TeV scale (since in our scans we are considering scalar masses up to ~ 1 TeV), and thus the presence of these high-energy operators is not expected to be of much help in case a runaway field direction exist at tree level in the 2HDM scalar potential.

4 Parameter grid

4.1 Parameter scans on masses, couplings and mixing angles

Logic of how we proceeded

- Starting from benchmark 3 of [1]

- Mapping the kinematics and sensitivity of the model by scanning some of the various parameters
- Checking whether other existing models can be rescaled

4.1.1 Results of studies

Each of the signatures should have the following plots in the planes of the final recommendation:

- efficiency at parton level with simplified, published cuts
- total and fiducial cross-section at parton level
- 2 - 3 kinematic plots of what has been scanned that are most representative for the analysis (here the analysers decide, then we harmonize at the end)

Signatures:

- Mono-Z (lep/had)
- MonoH→bb
- Monojet
- ttbar+MET, with specific discussion about rescaling
- other signatures who have not yet presented at public meetings, in ATLAS and CMS

4.1.2 Studies of the $h(bb) + E_T^{\mathrm{miss}}$ signature

The studies of the $h(bb) + E_T^{\mathrm{miss}}$ channel presented here are based on MC simulations with version 2.4.3 of MadGraph 5 [11] using a Universal FeynRules Output [12] implementation of the 2HDM with a Yukawa sector of type II with DM mediator (2HDM+a), as provided by the authors of [1]. The NNPDF30_lo_as_0130 set of parton distribution functions (PDF) at leading order in the five-flavor scheme, which assumes a massless b-quark, with $\alpha_S(m_Z) = 0.130$ is used for these simulations [13]. For consistency, five-flavor scheme and $m_b = 0$ GeV are chosen for the matrix element (ME) computation in MadGraph 5.

The ME generated for the parton-level studies presented in the following is $gg \to h\chi\chi$ represented in **??** The only exception is the $M_a - \tan\beta$ scan which will be discussed in the following and is summarised in Figure 12. In this scan also the ME $bb \to h\chi\chi$ is generated because at high $\tan\beta$, the bb initiated process can have an amplitude of a similar magnitude as the gluon fusion initiated process from **??** [1]. The gluon fusion is dominant in all the remaining parameter space, therefore the bb initiated process and other negligible contributions are not considered explicitly for all the scans.

Signal kinematics The free parameters of the 2HDM+a model fall into two categories:

- those which only affect total signal cross section;
- those which, in additional to the total cross section, also affect the kinematics, primarily the E_T^{miss} distribution.

In the following, the free parameters of the 2HDM+a model are studied in the context of the $h(bb)+E_T^{\text{miss}}$ signature with a particular focus on the latter category of parameters, as it emphasizes the kinematic diversity of potential new physics contributions represented in this simplified model.

The masses M_A and M_a of the pseudoscalars A and a, which represent the two mediators in **??**, affect the kinematics of the $h(bb)+E_T^{\text{miss}}$ in a profound way by changing the location of the Jacobian peak in the E_T^{miss} distribution. This effect is crucial to searches for $h(bb)+E_T^{\text{miss}}$ such as [14], since the E_T^{miss} observable can be used to reduce many SM backgrounds, which are typically characterised by low E_T^{miss}, unlike DM signal processes with potentially very high E_T^{miss}. In other words, the distribution of E_T^{miss} determines the sensitivity of the search.

The Jacobian peak is the result of a resonantly produced pseudoscalar A decaying in the $2\to1\to2$ process $gg\to A\to ah$, where the Higgs boson proceeds to decay into a visible final state as $h\to bb$, and the light pseudoscalar into an invisible one as $a\to\chi\chi$. Thus, the resonant $A\to ah$ process has a sharply peaked resonance in the invariant mass distribution of the final state system with a width determined by the widths of a, A, and h. This results in a peak in the momentum distribution of the DM system and in its transverse component that is reconstructed as E_T^{miss} in the detector.

Since it is determined by the masses of the particles involved in the decay, the location of the Jacobian peak can be calculated analytically [1]:

$$E_T^{\text{miss},max} \approx \frac{\sqrt{\left(M_A^2-M_a^2-M_h^2\right)^2-4M_a^2M_h^2}}{2M_A}\,. \tag{4.1}$$

Thus, increasing M_A results in a Jacobian peak at higher E_T^{miss}, as shown in Figure 2. Conversely, models with higher M_a have a Jacobian peak at lower E_T^{miss}, as indicated in Figure 3.

In conclusion, the M_A and M_a parameters strongly affect the sensitivity of a search for the 2HDM+a model using the $h(bb)+E_T^{\text{miss}}$ signature because they determine the location of the Jacobian peak in the E_T^{miss} distribution. Therefore, one of the proposed parameter scans for the 2HDM+a model is in the (M_a,M_A) plane.

Some fraction of signal events is due to non-resonant $2\to3$ processes $gg\to h\chi\chi$ which is represented in **??**. Due to the larger number of kinematic degrees of freedom, the invariant mass of the final state system is broadly distributed in these processes. Consequently, this results in a broad and soft E_T^{miss} distribution that is clearly distinct from the Jacobian peak discussed above. The models shown in Figure 2 and Figure 3 also have small contributions from non-resonant processes.

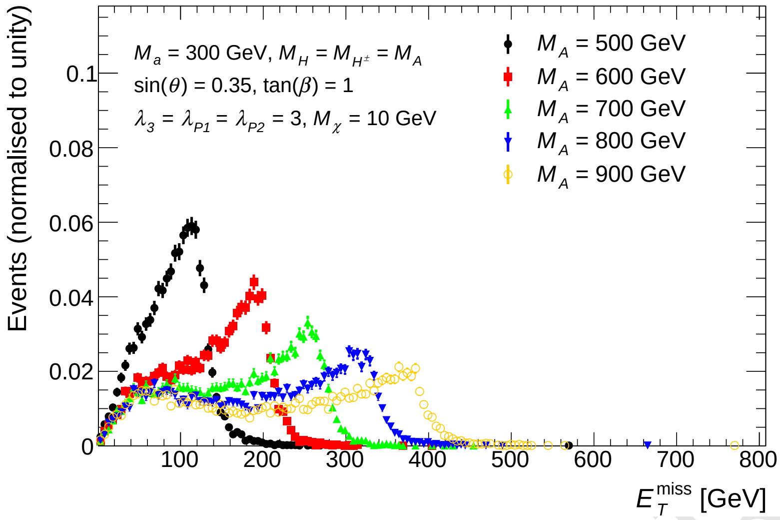

Figure 2: Missing transverse momentum distribution $h(bb) + E_T^{\text{miss}}$ signal events at parton level for five representative models with different $M_A(= M_H = M_{H^\pm})$ and fixed $M_a = 300$ GeV, $\sin\theta = 0.35, \tan\beta = 1, M_\chi = 10$ GeV and $\lambda_{P1} = \lambda_{P2} = \lambda_3 = 3$. Models with a larger $M_A - M_a$ splitting have harder E_T^{miss} (cf. Equation 4.1).

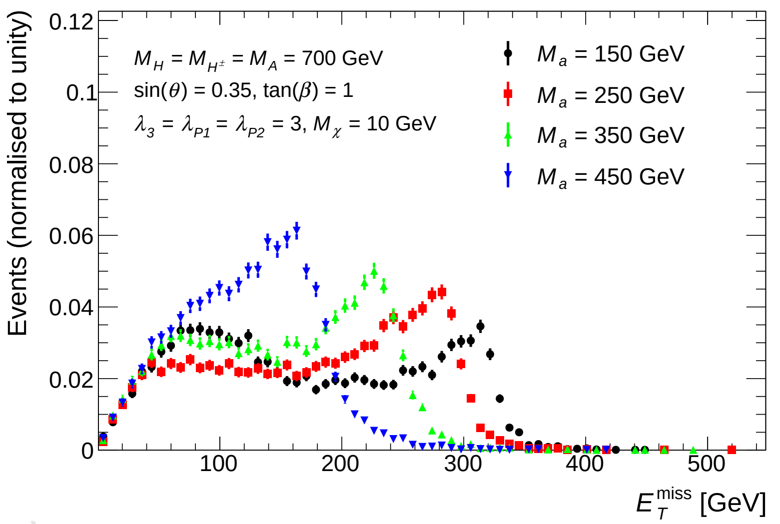

Figure 3: Missing transverse momentum distribution in $h(bb) + E_T^{\text{miss}}$ signal events at parton level for four representative models with different M_a and fixed $M_A = M_H = M_{H^\pm} = 700$ GeV, $\sin\theta = 0.35, \tan\beta = 1, M_\chi = 10$ GeV and $\lambda_{P1} = \lambda_{P2} = \lambda_3 = 3$. Models with higher M_a have softer E_T^{miss} (cf. Equation 4.1).

The mass of the heavy neutral scalar Higgs boson H has an indirect effect on the rate and kinematics of the signal. This is caused by the dependence of the coupling strengths and thus decay widths of the pseudoscalars A and a on M_H [1]. Therefore, a change of M_H can affect the relative contribution of resonant versus non-resonant signal processes, as

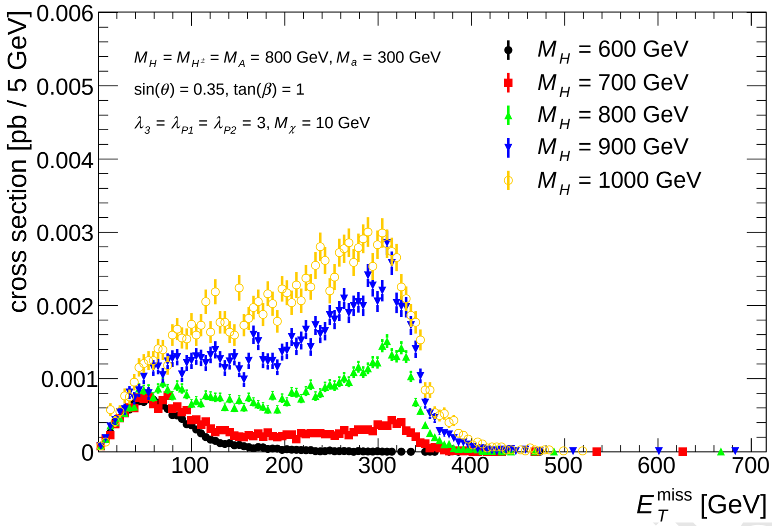

Figure 4: The E_T^{miss} distribution of the production cross section of $h(bb) + E_T^{\text{miss}}$ signal events for five representative models with different $M_H = M_{H^\pm}$ and fixed $M_A = 800$ GeV, $M_a = 300$ GeV, $\sin\theta = 0.35, \tan\beta = 1, M_\chi = 10$ GeV and $\lambda_{P1} = \lambda_{P2} = \lambda_3 = 3$.

illustrated in Figure 4. The choice $M_H = M_A$ results in a detectable total cross section for many signal points and a dominant contribution of the resonant signal process, resulting in diverse experimental signatures as demonstrated in Figure 2 and Figure 3. In addition, this choice results in about equal contributions to the sensitivity through the $Z+E_T^{\text{miss}}$ and $h+E_T^{\text{miss}}$ signatures, highlighting their complementarity. Henceforth, $M_H = M_A$ is adapted for all scans. For simplicity, the case of the neutral scalar $H^\pm$ being mass-degenerate to H is considered in the following, as it does not affect the 2HDM+a model kinematics in the $h(bb) + E_T^{\text{miss}}$ signature.

The sine of the mixing angle between the two pseudoscalars A and a, $\sin\theta$, affects not only the cross section, but also the shape of the E_T^{miss} distribution, as shown in Figure 5. For the resonant diagram $gg \to A \to ah \to \chi\bar{\chi}h$, the product of cross section times branching ratios $\mathcal{B}(A \to ah)\mathcal{B}(a \to \chi\bar{\chi})$ scales with $\sin^2\theta\cos^6\theta$, while for the diagram $gg \to a \to A^*h \to \chi\bar{\chi}h$, the product of cross section times branching ratios $\mathcal{B}(a \to Ah)\mathcal{B}(A \to \chi\bar{\chi})$ scales with $\sin^6\theta\cos^2\theta$. Therefore, at small $\sin\theta$, the resonant diagram $A \to ah$ is the dominant production mode and the E_T^{miss} distribution has a Jacobian peak following Equation 4.1; while at large $\sin\theta$, the $a \to A^*h$ diagram starts to dominate and produces a second peak at a lower E_T^{miss} value.

The shape of E_T^{miss} distribution also has a non-trivial dependence on $\tan\beta$, as can be seen in Figure 6. As discussed in the sensitivity study later, at small $\tan\beta$, the Yukawa coupling to top quark is large and the signal production mode is dominated by the non-resonant 3-body processes $gg \to h\chi\bar{\chi}$, which gives a broad and soft E_T^{miss} spectrum. As $\tan\beta$ increases, the contribution of resonant production increases as well and the Jacobian peak also appears. When the pseudoscalar A is produced off-shell, i.e. when $M_A < M_a + M_h$, the shapes of E_T^{miss} distributions become similar and the dependence on $\tan\beta$

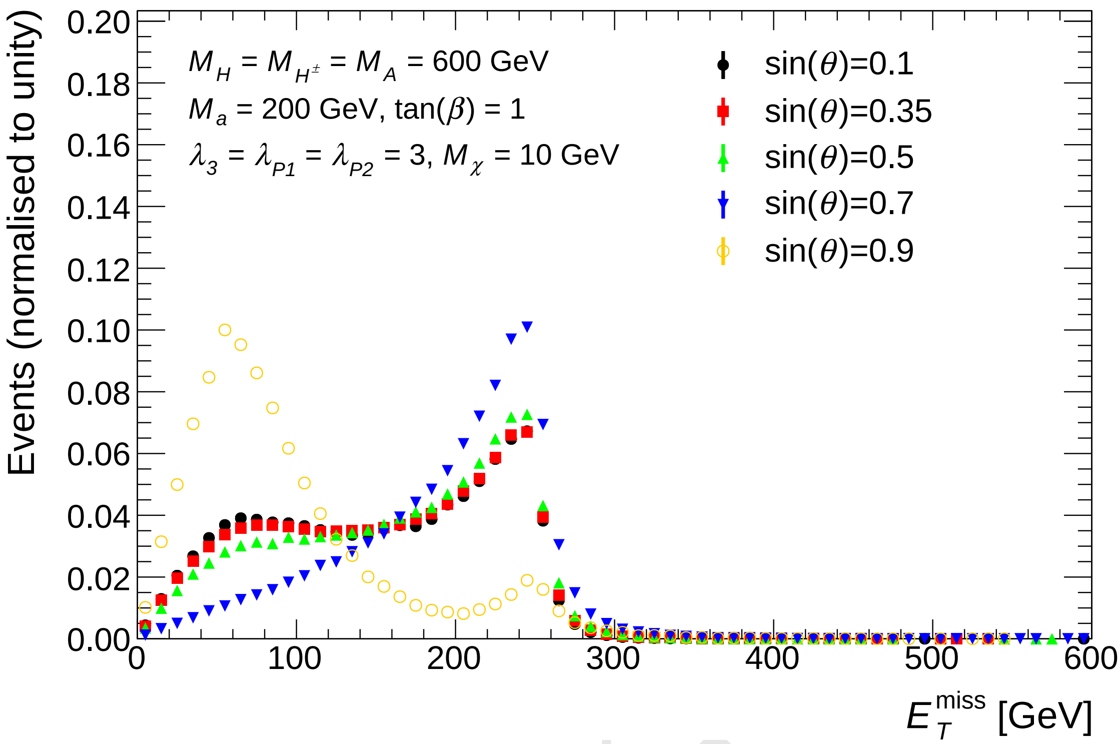

Figure 5: Missing transverse momentum distribution of $h \to bb + E_T^{\text{miss}}$ signal events at parton level for five representative models with different $\sin\theta$ and fixed $M_A = M_H = M_{H^\pm} = 600$ GeV, $M_a = 200$ GeV, $M_\chi = 10$ GeV, $\tan\beta = 1$, and $\lambda_{P1} = \lambda_{P2} = \lambda_3 = 3$. The shape of the E_T^{miss} distribution does not change much for $\sin\theta < 0.7$, then changes significantly for $\sin\theta \geq 0.7$. When $\sin\theta = 0.9$, the diagram $gg \to a \to A^*h \to \chi\bar{\chi}h$, producing a E_T^{miss} peak at around 60 GeV, starts to dominate.

disappears.

The mass of the DM fermion M_χ can change the total cross section and shape of the E_T^{miss} distribution, depending on the mass hierarchy of the A, a, h, χ particles. This is demonstrated in Figure 7. Provided on-shell decays $a \to \chi\chi$ are possible, i.e., $M_\chi < M_a/2$, the exact value of M_χ has no effect on either kinematics or the total cross section. The only exception is the case $M_a/2 > M_\chi > \frac{1}{2}(M_a - M_h)$. In this M_χ range, the non-resonant process $a \to hA^*\,(\chi\chi)$ is kinematically inaccessible. This reduces the overall cross section relative to the $M_\chi \leq \frac{1}{2}(M_a - M_h)$ case, and slightly changes the soft part of the total E_T^{miss} spectrum. But since the contribution of the $a \to hA^*\,(\chi\chi)$ is minor in any case, the differences are negligible.

If the DM particle mass is exactly on threshold, i.e., $M_\chi = M_a/2$, the total cross section is resonantly enhanced. This resonant threshold enhancement drops rapidly towards both higher and lower M_χ. Furthermore, the shape of the E_T^{miss} distribution at threshold, where amplitudes involving $a \to \chi\chi$ decays make up a larger fraction of the signal, differs significantly from the one below threshold. Below threshold ($M_\chi > M_a/2$), the total cross

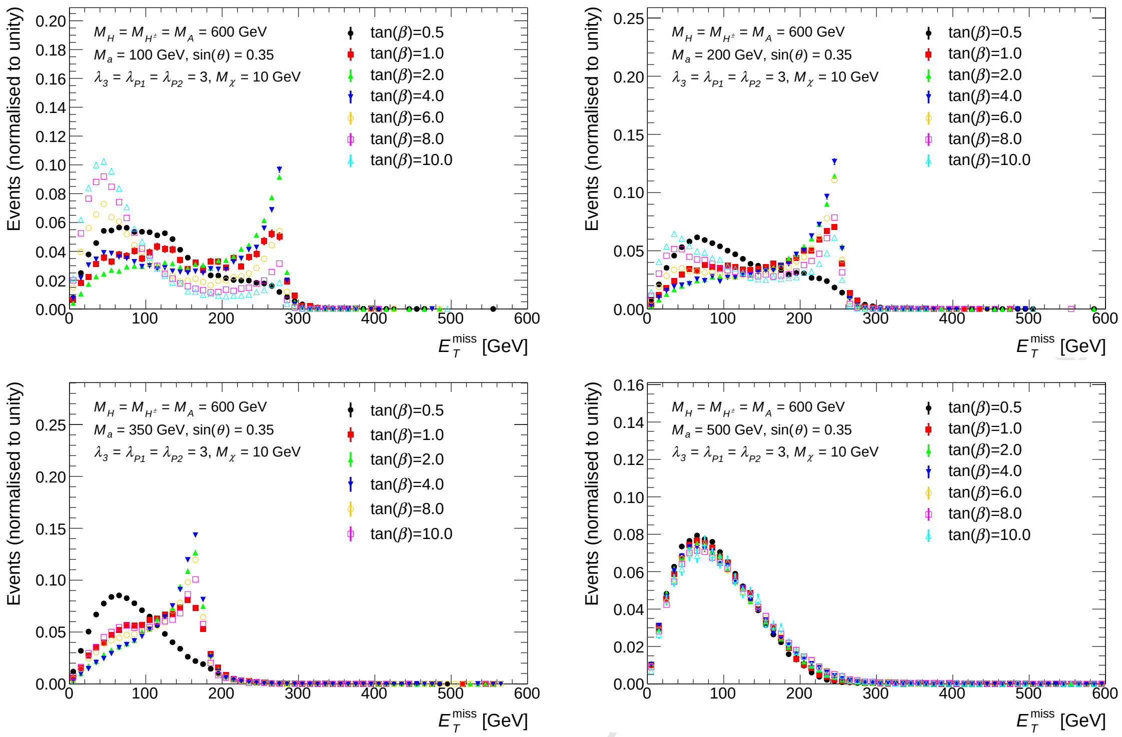

Figure 6: Missing transverse momentum distribution of $h \to bb + E_T^{\text{miss}}$ signal events at parton level with different $\tan\beta$ and fixed $M_A = M_H = M_{H^\pm} = 600$ GeV, $M_\chi = 10$ GeV, $\sin\theta = 0.35$, and $\lambda_{P1} = \lambda_{P2} = \lambda_3 = 3$. The values of M_a are set to 100, 200, 350, and 500 GeV, respectively. The shapes of the E_T^{miss} distributions for different $\tan\beta$ are similar when $M_A < M_h + M_a$. Note, in these figures, both the contributions of gg and $b\bar{b}$ initiated processes are included and a combined histogram is produced according to their corresponding cross sections.

section quickly drops by several orders of magnitude. In this regime, the shape of the E_T^{miss} distribution changes with M_χ continuously.

Sensitivity estimate The sensitivity estimate of ATLAS and CMS to the 2HDM+a scenario through the $h(bb) + E_T^{\text{miss}}$ signature is based on limits on anomalous production of 125 GeV Higgs bosons in association with E_T^{miss} with minimal model dependence [14]. The limits are translated to parton level and compared to parton-level simulations of the 2HDM+a scenario for the sensitivity estimate. This approach avoids the simulation of the detector response, which requires a significant amount of computing resources, and more iterations and refinements of the signal grid can be performed.

The limits with minimal model dependence are provided in terms of the detector-level cross section of $h(bb) + E_T^{\text{miss}}$ events $\sigma_i^{\text{obs}, h(bb)+E_T^{\text{miss}}}$ as a function of E_T^{miss} in four bins $i = 1, ...4$ [14]. To compare these values to the simulation results at parton level, an estimate of the detection efficiency ε times the kinematic acceptance $\mathcal{A}$ of the event selections of the analysis is used for each of the four E_T^{miss} bins. Thus, the $(\mathcal{A} \times \varepsilon)_i$ figure represents

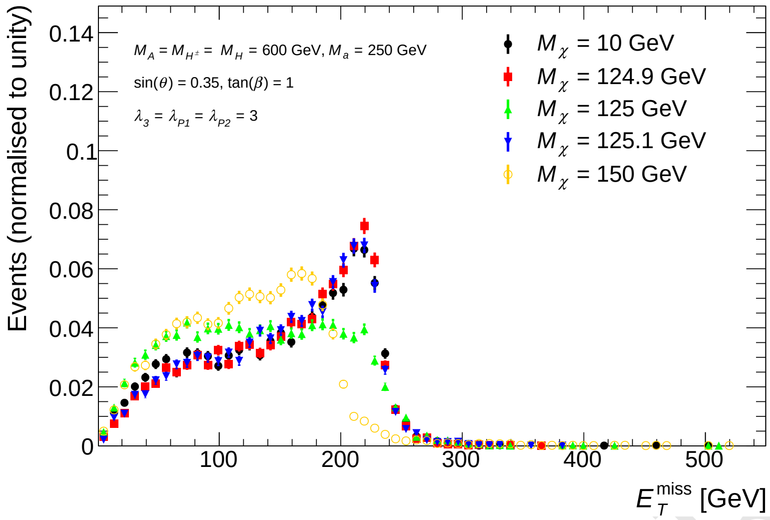

Figure 7: Missing transverse momentum distribution of $h(bb) + E_T^{\text{miss}}$ signal events at parton level for five representative models with different M_χ and fixed $M_A = M_H = M_{H^\pm} = 600$ GeV $M_a = 250$ GeV, $\sin\theta = 0.35, \tan\beta = 1$ and $\lambda_{P1} = \lambda_{P2} = \lambda_3 = 3$. The shape of the E_T^{miss} distribution does not change for $M_\chi < M_a/2$, then changes significantly for $M_\chi >= M_a/2$.

the minimum probability that an event generated at parton level in a given E_T^{miss} bin i is reconstructed in that same E_T^{miss} bin and passes all analysis selections. Consequently, the cross section for $h+$DM production in the 2HDM+a scenario at parton level $\sigma_i^{\text{parton}, h+\text{DM}}$ is calculated in the same E_T^{miss} bins as used in the $h(bb) + E_T^{\text{miss}}$ search. This starting point is shown in Figure 8 using the scan in (M_A, M_a) as a representative example. In the next step, the sensitivity $\mathcal{S}_i$ for each of the E_T^{miss} bins $i = 1, ...4$ is calculated as

$$\mathcal{S}_i \equiv \frac{\sigma_i^{\text{parton}, h+\text{DM}} \times \mathcal{B}^{\text{SM}, h\to bb} \times (\mathcal{A} \times \varepsilon)_i}{\sigma_i^{\text{obs}, h(bb)+E_T^{\text{miss}}}}\,, \tag{4.2}$$

where $\mathcal{B}^{\text{SM}, h\to bb}$ is the $h \to bb$ branching ratio predicted by the SM for the 125 GeV Higgs boson. A representative example for this step is given in Figure 9 for the scan in (M_A, M_a). A particular point in the (M_A, M_a) parameter parameter space is excluded if $\mathcal{S}_i \geq 1$. Finally, to obtain a single estimate for the total sensitivity $\mathcal{S}_{\text{tot}}$ using all four E_T^{miss} bins, their individual contributions from Equation 4.2 are summed over[2]:

$$\mathcal{S}_{\text{tot}} \equiv \sum_{i \in E_T^{\text{miss}} \text{ bins}} \mathcal{S}_i\,. \tag{4.3}$$

[2] This choice is made because the individual per-bin sensitivities follow a logarithmic metric, and because a model will typically populate several E_T^{miss} bins at a time. This implies that there could be models where $\mathcal{S}_i < 1$ in every bin, yet the sum from Equation 4.3 is > 1. Therefore, for a rigorous exclusion of a model based on the limits with minimal model dependence, the preferred approach would be to consider only the most sensitive bin for the exclusion.

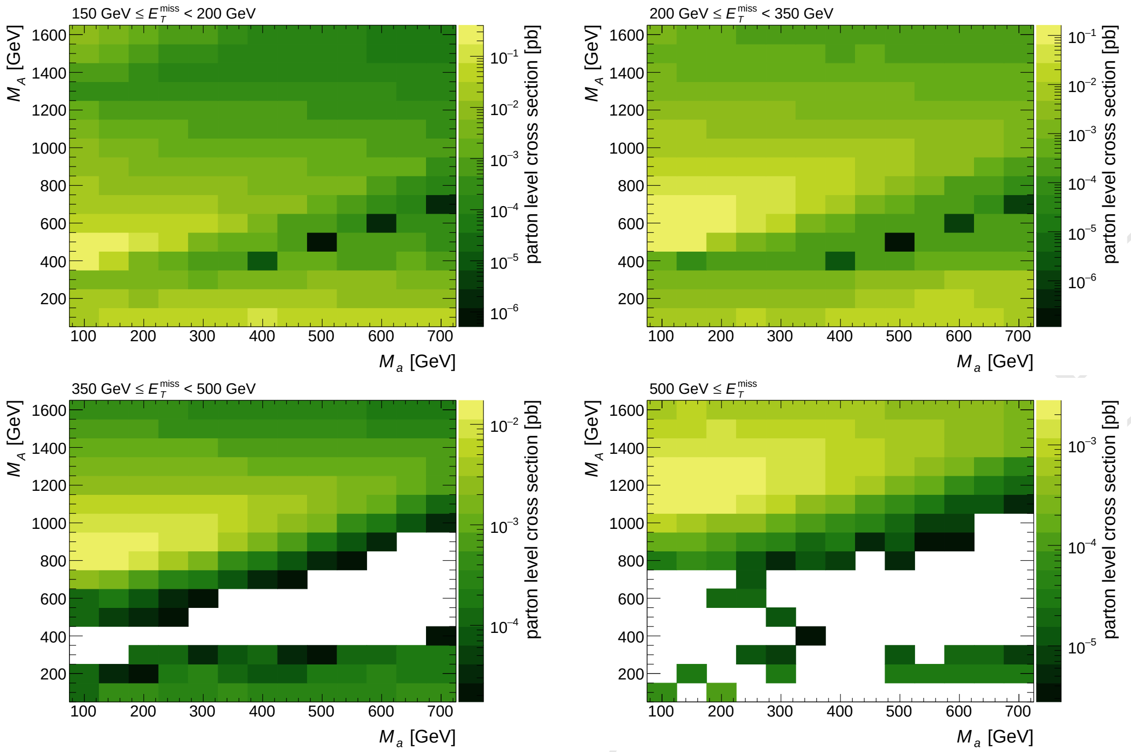

Figure 8: The production cross section of $h \to bb + E_T^{\rm miss}$ signal events at parton level as a function of (M_A, M_a) in each of the four $E_T^{\rm miss}$ bins. The remaining parameters take the values $M_H = M_{H^\pm} = M_A, \sin\theta = 0.35, \tan\beta = 1, M_\chi = 10$ GeV and $\lambda_{P1} = \lambda_{P2} = \lambda_3 = 3$.

The resulting $\mathcal{S}_{\rm tot}$ is shown in Figure 10 for the example of the (M_A, M_a) scan.

The scan of the sensitivity in the sense of Equation 4.3 in the (M_a, M_A) plane is shown in Figure 10. The sensitivity decreases with increasing $M_A = M_H = M_{H^\pm}$ for $M_A \geq 1$ TeV because the fraction of resonant signal events drops. This drop is caused by increasingly large Γ_A, which allows for an increasing fraction of non-resonant signal events, driven by events with very off-shell A. Near the mass diagonal $M_a = M_A$, there is little to no sensitivity. This is because the Jacobian peak moves to low $E_T^{\rm miss}$ for a small mass splitting $|M_A - M_a|$ (Equation 4.1, Figure 2, and Figure 3). Beyond this, the coupling g_{Aah} is small when all Higgs bosons are nearly degenerate in mass, cf. Equation 4.12 in Ref. [1], resulting in a small total cross section and therefore further decrease in sensitivity. The sensitivity above the mass diagonal, $M_A > M_a$, is larger than below the mass diagonal. Two parameter choices cause this asymmetry:

1. $M_A = M_H = M_{H^\pm}$, i.e., the neutral and charged CP-even scalars have low masses below the diagonal, but high masses above it, introducing an asymmetry. Another effect can be seen in Figure 4: values of $M_H = M_{H^\pm}$ below the mass of the higher-mass pseudoscalar (in this case A) give a reduced total cross section and a lower fraction of resonant signal events. Both effects reduce sensitivity;

2. $\sin\theta = 0.35 \neq 1/\sqrt{2}$, i.e. the mixing between the pseudoscalars A and a is asymmet-

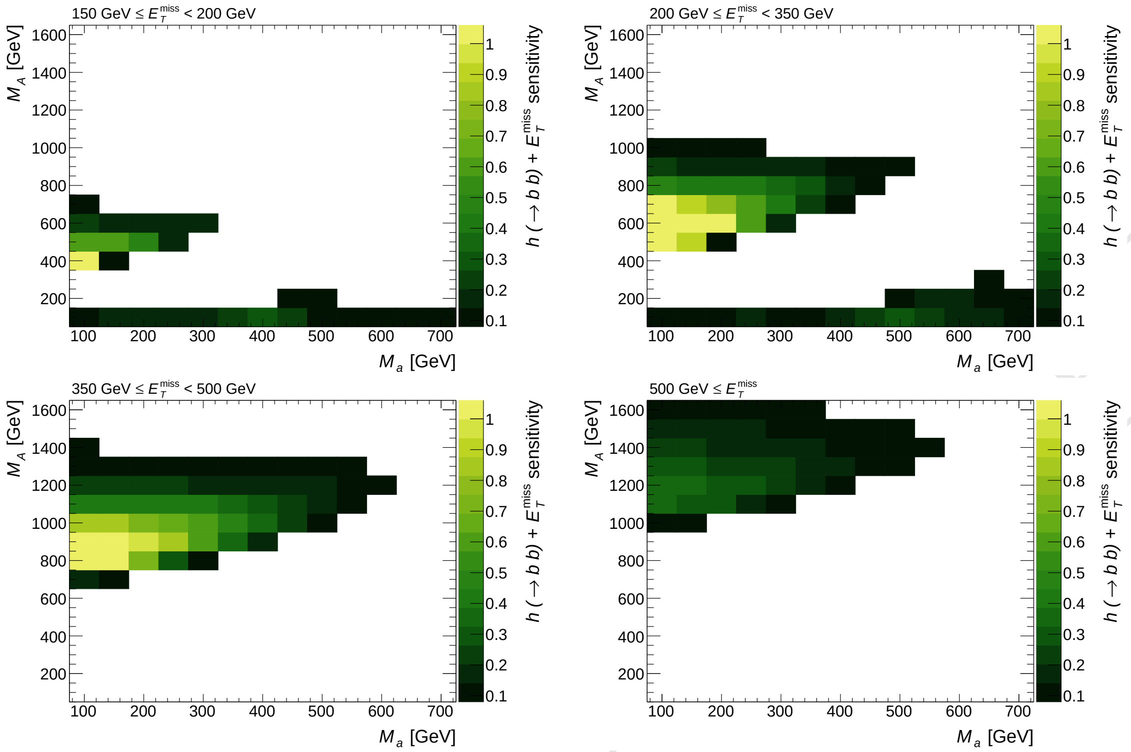

Figure 9: Estimated sensitivity to $h \to bb + E_T^{\rm miss}$ events as a function of (M_A, M_a) in each of the four $E_T^{\rm miss}$ bins. The sensitivity, defined in Equation 4.3, is based on the limits with reduced model dependence from Ref. [14]. The remaining parameters take the values $M_H = M_{H^\pm} = M_A, \sin\theta = 0.35, \tan\beta = 1, M_\chi = 10$ GeV and $\lambda_{P1} = \lambda_{P2} = \lambda_3 = 3$.

ric. A couples more strongly to SM particles than a, and vice versa for the couplings to the DM fermion χ. So the situation below the diagonal corresponds to the case of $\sin\theta = \sqrt{1 - 0.35^2} \approx 0.938$ and $M_A > M_a$. As can be seen in Figure 5, this $\sin\theta$ configuration has a higher fraction of non-resonant signal events with low $E_T^{\rm miss}$, and correspondingly a lower sensitivity is found in Figure 11.

The scan of the sensitivity in the $(M_a, \tan\beta)$ plane is shown in Figure 12. At very low $\tan\beta$, the Yukawa coupling to top quarks is large, and most of the signal events come from non-resonant processes, as can be seen from Figure 6. The non-resonant processes are characterised by soft $E_T^{\rm miss}$, which lowers the kinematic acceptance and reduces the sensitivity of the search. For higher $\tan\beta$, the fraction of resonant events increases due to the reduced top Yukawa coupling, resulting in an increase of sensitivity. However, reducing the top Yukawa coupling also reduces the total production cross section. This effect is sub-dominant below $\tan\beta \approx 1.2$, and the sensitivity increases with $\tan\beta$. But above $\tan\beta \approx 1.2$, the sensitivity loss due to reduced cross section outpaces the sensitivity gain due to a more resonant signal. Overall, the search gets less sensitive with increasing $\tan\beta$ above $\tan\beta \approx 1.2$. At very high $\tan\beta$ (≥ 10), this trend is reversed again because the $\tan\beta$

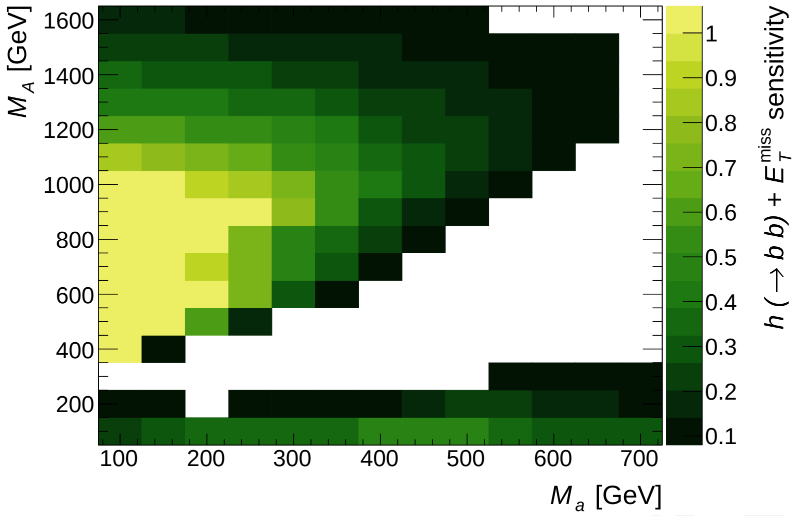

Figure 10: Sum over all E_T^{miss}-bins of the estimated sensitivity to $h \to bb + E_T^{\text{miss}}$ events as a function of (M_A, M_a). The sensitivity, defined in Equation 4.3, is based on the limits with reduced model dependence from Ref. [14]. The remaining parameters take the values $M_H = M_{H^\pm} = M_A, \sin\theta = 0.35, \tan\beta = 1, M_\chi = 10$ GeV and $\lambda_{P1} = \lambda_{P2} = \lambda_3 = 3$.

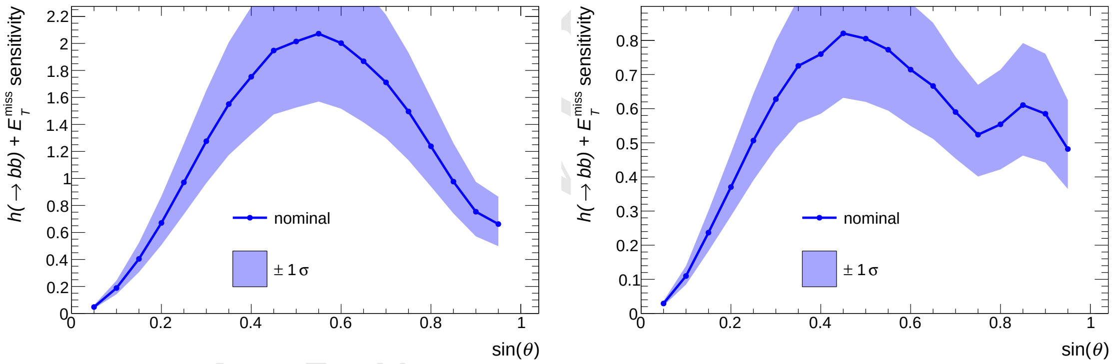

Figure 11: Sum over all E_T^{miss}-bins of the estimated signal sensitivity to $h \to bb + E_T^{\text{miss}}$ events as a function of the pseudoscalar mixing parameter $\sin\theta$, for $M_a = 200$ GeV and $M_H = M_{H^\pm} = M_A = 600$ GeV (left) as well as $M_a = 350$ GeV and $M_H = M_{H^\pm} = M_A = 1000$ GeV (right). The remaining parameters take the values $M_\chi = 10$ GeV, $\tan\beta = 1$, and $\lambda_{P1} = \lambda_{P2} = \lambda_3 = 3$. The sensitivity, defined in Equation 4.3, as well as the uncertainty on the sensitivity (shaded blue) are based on the limits with reduced model dependence from Ref. [14] and the uncertainties described therein.

enhancement[3] of the coupling to b-quarks compensates for the small b-quark mass. At this point bb initiated processes start to dominate the production cross section and drive the increase in sensitivity.

The sensitivity to models with varying $\sin\theta$ is shown in Figure 11. The sensitivity

[3] The 2HDM+a scenario assumes a Yukawa sector of type II.

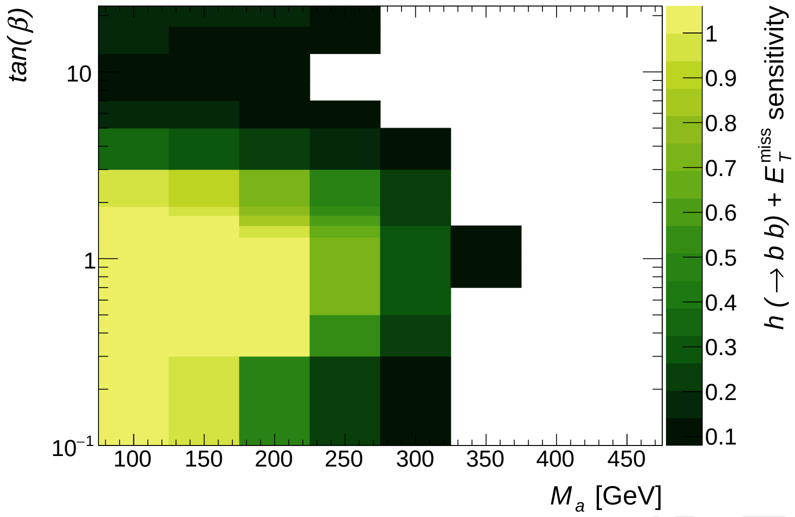

Figure 12: Sum over all E_T^{miss}-bins of the estimated signal sensitivity to $h \to bb + E_T^{\text{miss}}$ events as a function of $(M_a, \tan\beta)$. The sensitivity, defined in Equation 4.3, is based on the limits with reduced model dependence from Ref. [14]. The remaining parameters take the values $M_H = M_{H^\pm} = M_A = 600$ GeV, $\sin\theta = 0.35$, $M_\chi = 10$ GeV and $\lambda_{P1} = \lambda_{P2} = \lambda_3 = 3$.

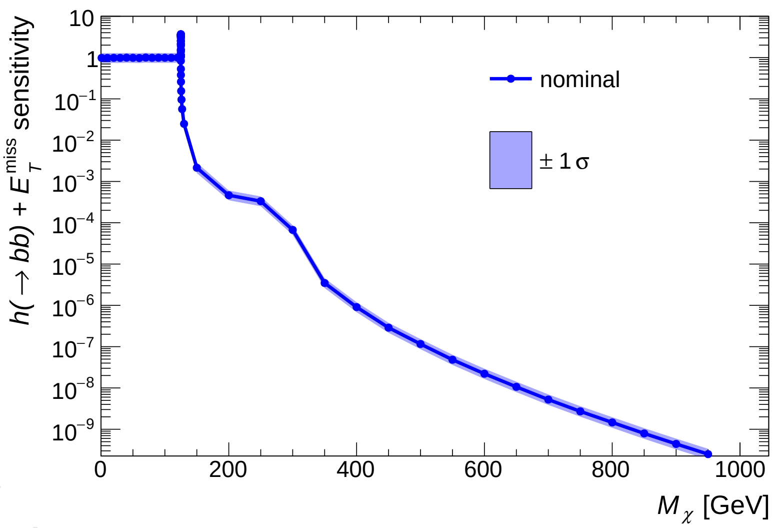

Figure 13: Sum over all E_T^{miss}-bins of the estimated signal sensitivity to $h \to bb + E_T^{\text{miss}}$ events as a function of the DM mass M_χ. The sensitivity, defined in Equation 4.3, as well as the uncertainty on the sensitivity (shaded blue) are based on the limits with reduced model dependence from Ref. [14] and the uncertainties described therein. The remaining parameters take the values $M_a = 250$ GeV$, M_H = M_{H^\pm} = M_A = 600$ GeV, $\sin\theta = 0.35, \tan\beta = 1$, and $\lambda_{P1} = \lambda_{P2} = \lambda_3 = 3$. The sensitivity is constant below $M_\chi < M_a/2$, and rapidly drops for $M_\chi > M_a/2$. The sensitivity is resonantly enhanced for $M_\chi = M_a/2$.

vanishes at $\sin\theta = 0$ and $\sin\theta = 1$, since those values correspond to no mixing between A and a, and thus no connection between the SM and the dark sector. For its intermediate values, the $\sin\theta$ parameter influences the couplings of the pseudoscalars to DM as well as to SM fermions, and also the coupling strength of trilinear scalar vertices such as g_{Aah} [1]. Increasing the couplings increases the total cross section. However, increasing some couplings can also increase Γ_A and thereby decrease the resonant fraction of signal events and the sensitivity. The upshot of this is that there can be more than one local maximum in the sensitivity curve, as shown the right panel of Figure 11. The precise dependence of the sensitivity on $\sin\theta$ depends on the precise interplay of the couplings. Because the couplings depend on all other model parameters including all the Higgs masses, tuning the $\sin\theta$ of a parameter scan to the sensitivity in a single point can lead to sub-optimal sensitivity in other points.

The sensitivity to models with varying M_χ is shown in Figure 13. Below the threshold of $M_\chi < M_a/2$, the sensitivity is constant since the $E_T^{\rm miss}$ distribution and the total signal cross section remain invariant, as demonstrated in Figure 7. At threshold, the sensitivity is enhanced because the partial width for $a \to \chi\chi$ is enhanced, increasing the signal cross section. Above threshold, the sensitivity drops rapidly because $M_\chi > M_a/2$ requires an off-shell $a^\star \to \chi\chi$ decay, which is strongly suppressed by the typically narrow width of a. The width of a is substantially reduced once $a \to \chi\chi$ is kinematically inaccessible, as $\Gamma_{a\to\chi\chi}$ is a large contribution to the total width of a for $M_\chi \leq M_a/2$ [1]. There is a slight increase in sensitivity for $M_\chi \approx M_A/2$ when the $A \to \chi\chi$ decay hits its kinematic threshold, yet the absolute sensitivity remains negligible.

4.1.3 Studies of the mono-Z (leptonic) signature

Mono-Z analyses use events with a reconstructed Z boson recoiling symmetrically against $E_T^{\rm miss}$ to detect the production of invisible particles. In previous LHC analyses [15, 16], the DM interpretations of the analysis results have focused on either invisible decays of the SM-like Higgs bosons or topologies where the Z boson is produced as initial-state radiation (ISR) off a quark. The ISR-based topologies generically favor radiation of a gluon or photon rather than a massive gauge boson, thus limiting the discovery sensitive of a Z-based approach compared to monojet and mono-photon searches. In contrast, the model studies in this document generates the mono-Z signature dominantly via the all-bosonic H-a-Z vertex, which can lead to enhancements of the mono-Z sensitivity compared to jet and photon signature. In this section, the behavior and experimental accessibility of the model in Z+$E_T^{\rm miss}$ events is studied.

Technical setup Simulated event samples for the mono-Z signature are produced with Madgraph5_aMC@NLO version 2.4.3, interfaced with Pythia version 8.2.2.6 for parton showering. The NNPDF3.0 PDF set is used at LO precision with the value of the strong coupling constant set to $\alpha_S(M_Z) = 0.130$ (NNPDF30_lo_as_0130). Only contributions from gluon-gluon initial states and $l^+\ l^-\ \chi\overline{\chi}$ final states are considered, where l = e or μ. No additional matrix element partons are considered and diagrams with an intermediate s-

Table 1: Event selection requirements for the analysis of the Mono-Z signature with leptonic Z decays. The requirements are inspired to follow those used in typical experimental analyses.

Selection stage	Quantity	Requirement
Inclusive	lepton $\lvert\eta\rvert$	< 2.5
	leading (trailing) lepton p_T	$> 25(20)$ GeV
Preselection	$\lvert m_{ll} - m_{Z,\text{nominal}}\rvert$	< 15 GeV
	E_T^{miss}	> 40 GeV
Final selection	$\Delta\Phi(ll, E_T^{\text{miss}})$	> 2.7
	$\lvert p_{T,ll} - E_T^{\text{miss}}\rvert / p_{T,ll}$	< 0.4
	$\Delta R(ll)$	< 1.8

channel SM Higgs boson are explicitly rejected to increas the calculation efficiency (generate g g > xd xd l+ l- / h1).

Event selection Three consecutive stages of event selection are considered:

- Inclusive: Lepton p_T and η requirements corresponding to the typical experimental trigger acceptance are applied.
- Preselection: A dilepton candidate with an invariant mass in a window around the Z mass is required, and a minimum transverse momentum of the $\chi\overline{\chi}$ system is required.
- Final selection: Requirements on the main variables used in the relevant analyses are added: The angular separation in the transverse plane between the $\chi\overline{\chi}$ and l^+ l^- systems $\Delta\Phi(ll, E_T^{\text{miss}})$, the relative transverse momentum difference between them $\lvert p_{T,ll} - E_T^{\text{miss}}\rvert / p_{T,ll}$ and the angular separation between the leptons $\Delta R(ll)$. Additionally, the E_T^{miss} requirement is tightened.

The exact event selection criteria are listed in Tab. 1.

Cross-sections, kinematic distributions and acceptance The overall cross-sections in the $\tan\beta$ and mass scans are shown in Fig. 14. In the mass scan, maximal cross-sections are observed for the region of $M_a < M_A$ for values of $M_a \gtrsim 100$ GeV. Towards higher values of both M_a and M_A, the cross-sections fall off, reaching values smaller than 1 fb at $M_a \approx 450$ GeV or $M_A \approx 1.1$ TeV. In the $M_a \approx M_A$-region, the cross-section is suppressed by destructive interference. For the region with inverted mass hierarchy $M_a > M_A$, cross-sections of the order of multiple fb are observed, as long as $\lvert M_a - M_A\rvert$ remains sufficiently large. In the $\tan\beta$ scan, cross-sections smoothly fall with increasing M_a as well as $\tan\beta$. Cross-sections are typically larger than 1 fb up to $\tan\beta \approx 5$. The dependence on M_a is modulated by the value of $\tan\beta$: Crossing the M_a range from 100 to 400 GeV, cross-sections are reduced by a factor ≈ 7 for small $\tan\beta \approx 1$, but only a factor ≈ 2 for higher values of $\tan\beta \approx 5$.

Acceptances for the mass and $\tan\beta$ scans are shown in Figures 15 and 16. In the mass scan, from $M_a = 100$, $M_A = 250$ to $M_a = 350$, $M_A = 450$, we can see that for mass points where the Jacobian Peak is below the E_T^{miss} cut of the ananalysis, acceptances drop sharply approaching zero. Above this region, the acceptance curves are grouped into bands for fixed values of $M_A - M_a$. For large values of M_A, the acceptance changes more gradually and reaches a maximum value of 50%. In the inverted mass region, the acceptance is generally lower than in the rest of the mass scan, but can reach values as large as 30% for for light values of M_A. In the $\tan\beta$ scan, the acceptance is largely independent of $\tan\beta$ and is constant for equal values of M_a.

To assess the kinematic behavior of the signal, the distributions of the kinematic variables that are most relevant to the Mono-Z signature are studied as a function of the model parameters.

The distribution of the invariant masses of the dilepton and $\chi\chi$ systems are shown in Fig. 22. Independent of the of parameters, the dilepton mass spectrum is centered at the Z peak, without any nonresonant contribution. The $M_{\chi\chi}$ distribution illustrates the signal contributions from different diagrams. For $M_A > M_a$, DM is dominantly produced from on-shell a boson production. In the inverted mass region $M_A < M_a$, the situation is reversed, and H diagrams dominate.

After applying the preselection requirements, the distributions of kinematic variables are shown in Fig. 23. In the region of $M_A > M_a$, distinct Jacobian peaks are visible in the distributions of the mediator p_T, the width of which generally increases with values of M_a and M_A. Significant portions of the spectrum are situated at relatively high boosts ($E_T^{\text{miss}} > 200\,\text{GeV}$), which is more easily accessible experimentally. This behavior is contrasted by the distributions in the inverted mass regions, which show nearly no distinct features and are mainly located at low mediator p_T. For $M_A \approx M_a + m_Z$, both the a and Z bosons are produced approximately at rest, leading to an event population with overall low boost. These qualitative trends are consistent between the observables studied here. Finally, the distributions of the E_T^{miss} and M_T variables after final selection are shown in Fig. 24. Traditionally, the Mono-Z search has relied on the E_T^{miss} distribution for signal extraction. While the presence of the Jacobian peak structure in the distribution facilitates signal-background separation, it may be beneficial to also consider the M_T distribution. Although only transverse information is available, the resonant structure of the signal is significantly enhanced in the M_T variable, which may enhance the sensitivity of a specialized search strategy.

The $\tan\beta$ and $\sin(\theta)$ variables have minimal effect on the distributions of kinematic variables (Fig. **??**).

Conclusions The Mono-Z(ll) provides experimental coverage of the pseudoscalar 2HDM model for a broad part of the parameter space. The light pseudoscalar ąn be probed up to mass values of $\approx 350\,\text{GeV}$, depending on the choice of other parameters. The Mono-Z is sensitive mostly in the region of low values of $\tan\beta < 4$.

Expected significance Expected significances for 2HDMa models are calculated using generator level signal samples and background estimates from recent $Z(\ell\ell)+E_T^{\text{miss}}$ searches analyzing 36.1 fb^{-1} of data [15].

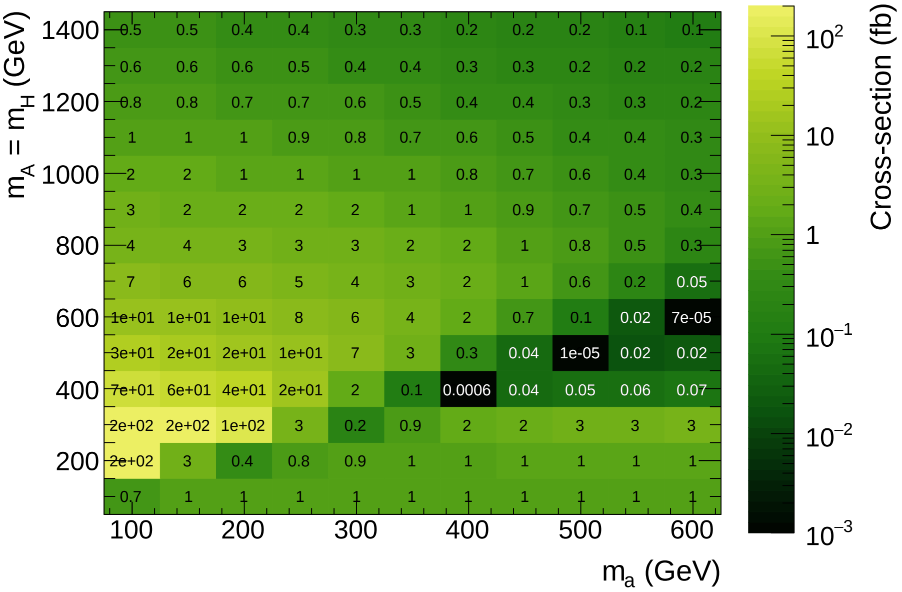

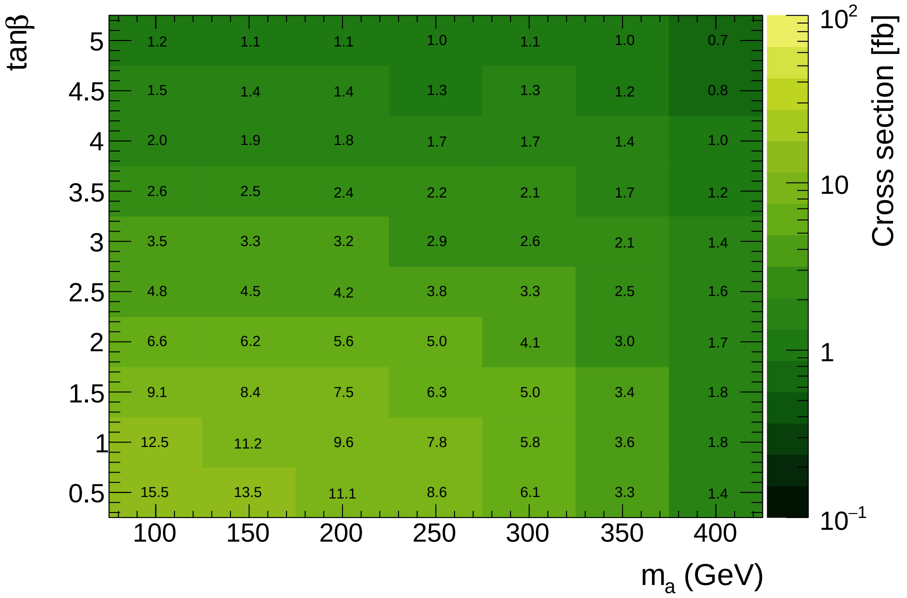

Figure 14: Inclusive cross-sections for $pp \to l^+l^-\chi\overline{\chi}$ in the M_a-M_A (top) and M_a-$\tan\beta$ scans (bottom).

Following the Asimov approximation, the expected significance for the ratio of likelihoods is given by equation 4.4 and is valid even for s not $\ll b$ [17]. This equation is modified to account for systematic uncertainties on the background (4.5) [18], and the total significance is taken as the per bin significances summed in quadrature.

For the signal events a reconstruction efficiency of 75% is assumed. To be consistent with the background estimates, the ATLAS selection cuts are used. The significances are calulated for bins of E_T^{miss}. A conservative 20% systematic is assumed for E_T^{miss} ¡ and 10%

for MET ¿.

The expected significances are shown in Figure 25, the LHC should be sensitive to models with a significance greater than 2.

$$Z = \sqrt{2\left((s+b)\ln 1 + \frac{s}{b} - S\right)} \tag{4.4}$$

$$Z'_{bin} = \sqrt{2\cdot\left((s+b)\ln[\frac{(s+b)(b+\sigma_b^2)}{b^2+(s+b)\sigma_b^2}] - \frac{b^2}{\sigma_b^2}\ln[1+\frac{\sigma_b^2 s}{b(b+\sigma_b^2)}]\right)} \tag{4.5}$$

$$\mathcal{S} = \sqrt{\sum_{bin}(Z'_{bin})^2} \tag{4.6}$$

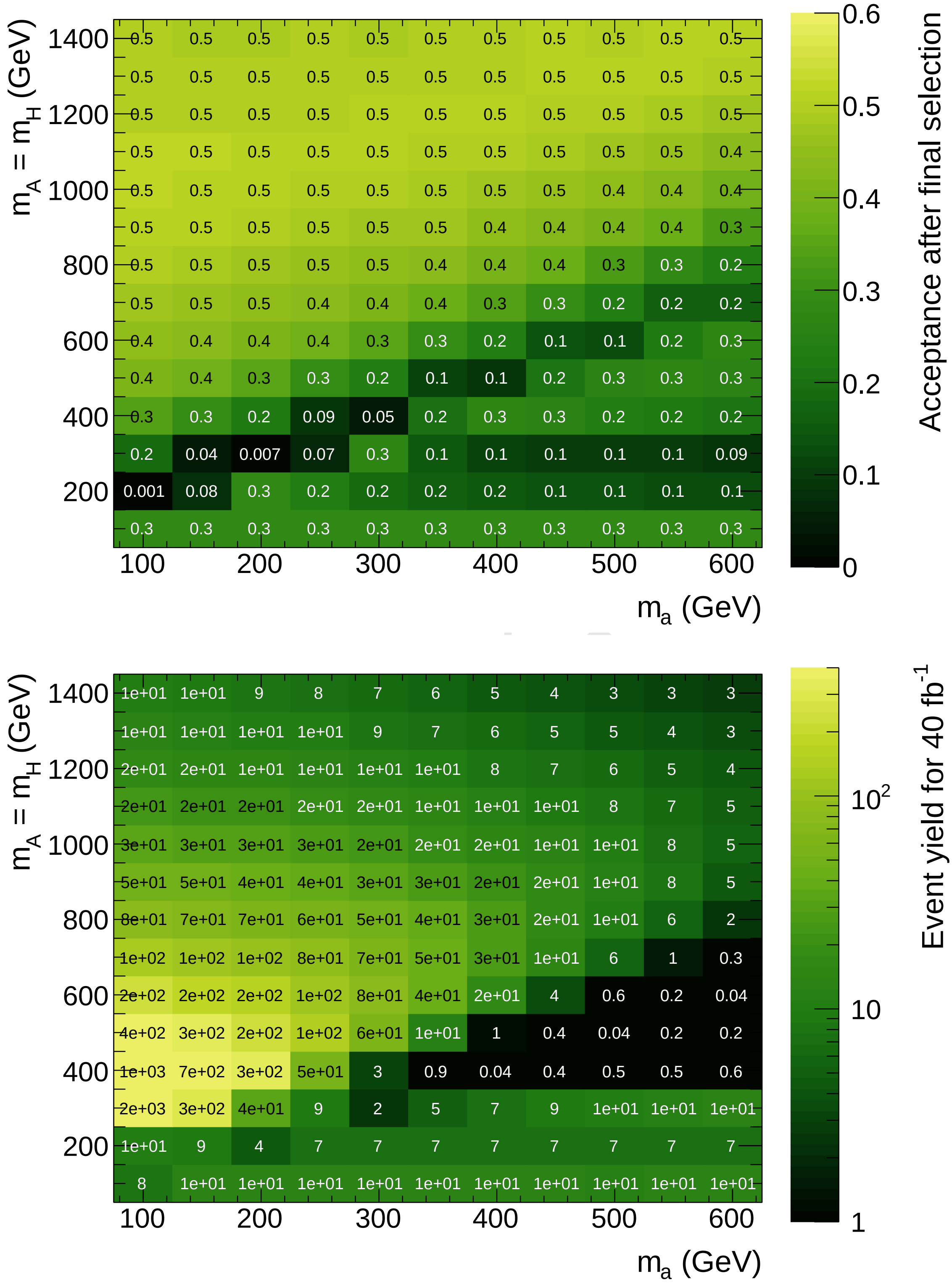

Figure 15: Acceptance and event yields in the M_a-M_A plane after applying the final selection. Event yields assume an integrated luminosity of 40 fb^{-1}. The acceptance is maximal for $M_A > M_a$, where it reaches 50 %. In the inverted mass region $M_A < M_a$, lower values of 10-30% are observed. In the intermediate region around $M_A \approx M_a + M_Z$, the acceptance is strongly suppressed as the a and Z bosons are produced approximately at rest.

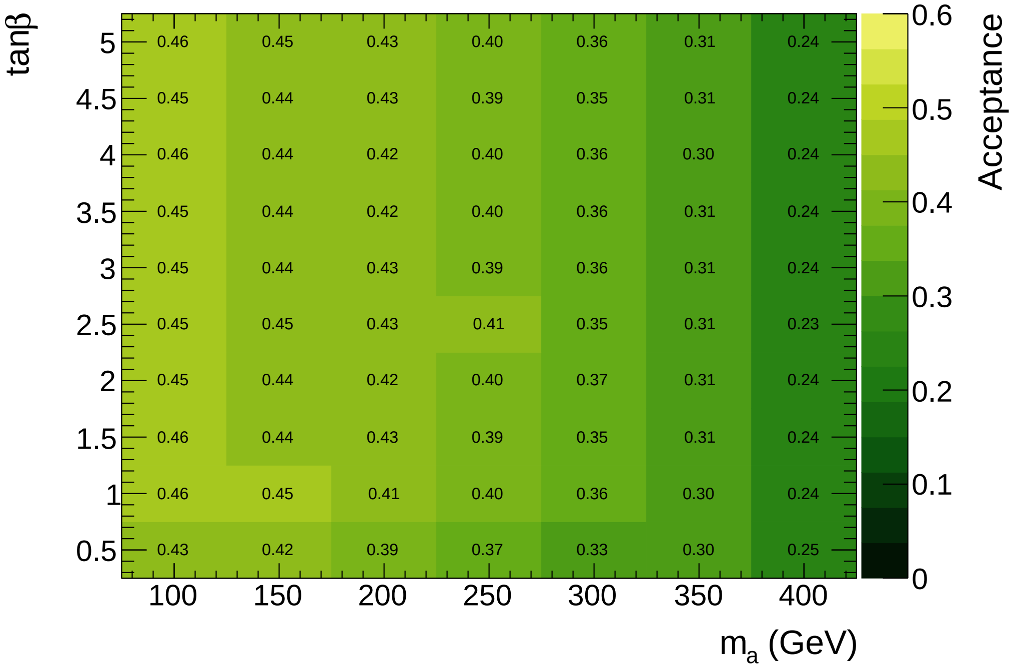

Figure 16: Acceptances across the M_a-tan β scan. Acceptance is flat over tan β for constant values of M_a.

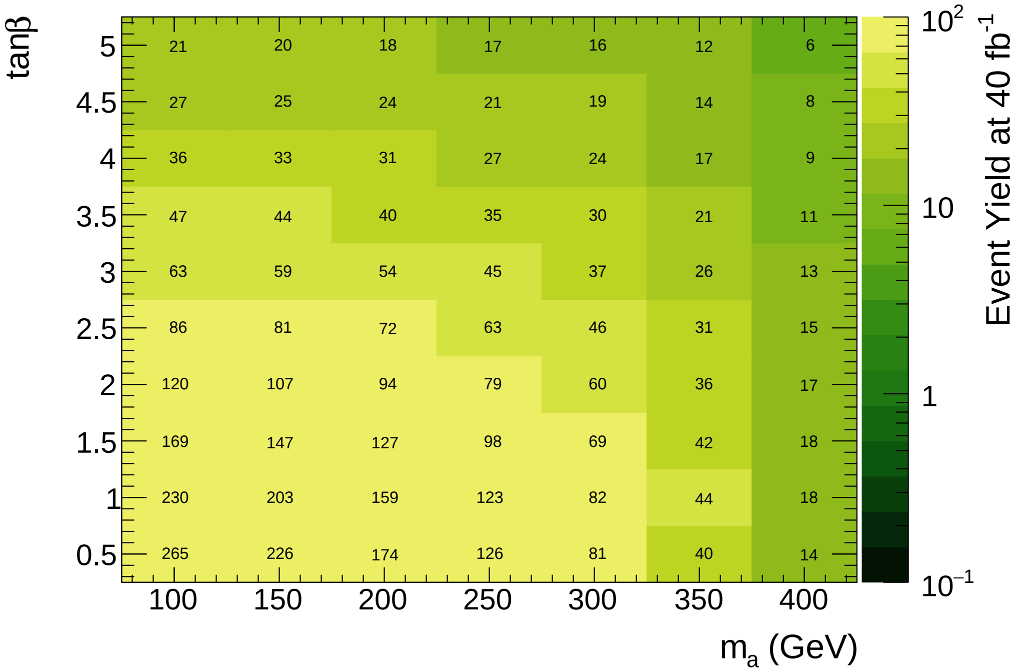

Figure 17: Event yield in the M_a-tanBeta grid, for an integrated luminosity of 40 fb^{-1}. The number of expected events diminshes with increasing tanBeta and M_a. M_A fixed to 600 GeV and sinTheta to 0.35

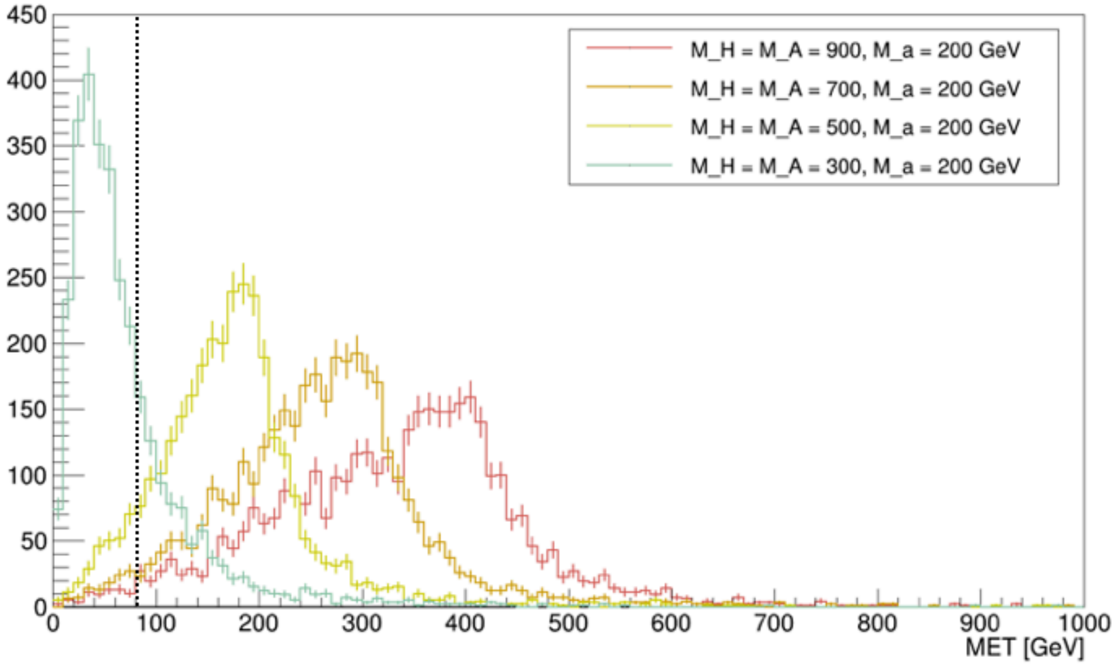

Figure 18: The position of the Jacobian peak in the E_T^{miss} distribution depends on the difference between M_H and M_a. For fixed values of M_a and $M_A = M_H$, increaseing M_A shifts the peak towards higher enrgies, and decreasing M_A shifts it lower. For small mass splittings between M_H and M_a, most events will fail to pass the E_T^{miss} selection criteria.

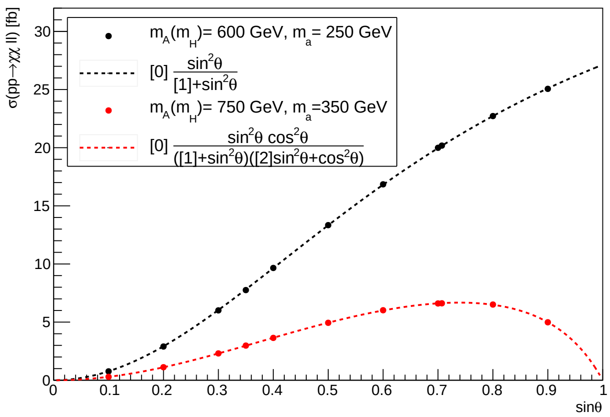

Figure 19: For two different mass points, this figure shows the cross section $pp \to \chi\chi\ell\ell$ as a function of $\sin\theta$. For $M_a < 350$ GeV, a decays solely to dark matter particles. As a consequence, the mixing angle only impacts the heavy scalar's branching fraction to aZ and cross section strictly increases with $\sin\theta$. For M_a above 350 GeV, $\bar{t}t$ decays become accesible, introducing additional $\sin\theta$ and $\cos\theta$ dependences for the branching fraction of $a \to \chi\chi$. Above 350 GeV for large values of $\sin\theta$, there is a turnover point where the reduced $a \to \chi\chi$ branching fraction outweights the increased $H \to aZ$ branching and the net cross section decreases.

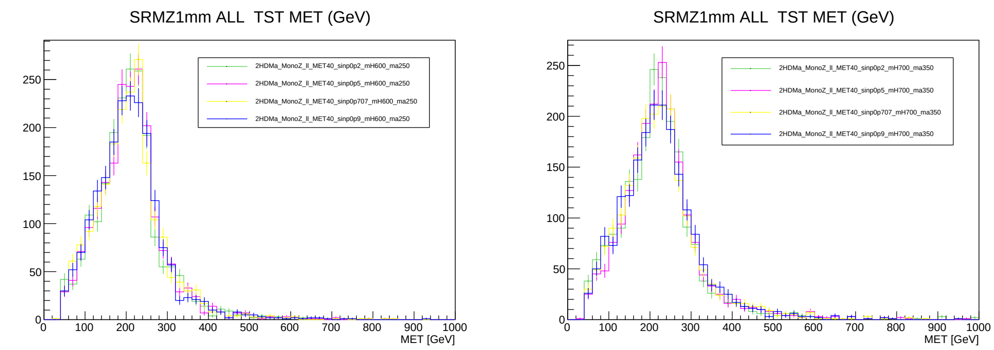

Figure 20: Performing one dimensional scans of sinTheta shows that it has little impact on the events' kinematic distributions. The first scan is performed at $M_A = 600$ GeV and $M_a = 250$ GeV, the second at $M_A = 700$ GeV $M_a = 350$ GeV. In both cases tanBeta = 1.0.

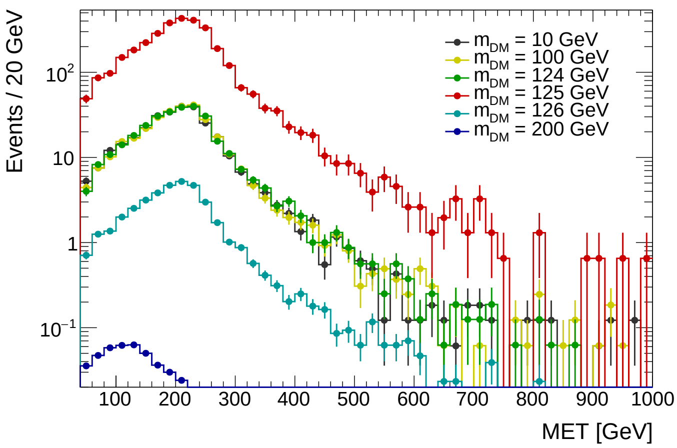

Figure 21: In the DM mass scan, for $M_\chi < \frac{M_H}{2}$, the DM mass has no effect on cross section or kinematic distributions, at $M_\chi = \frac{M_H}{2}$ a resonant enhancement to the cross section occurs, and in the off-shell region where $M_\chi > \frac{M_H}{2}$ cross section steeply drops and the $E_T^{\rm miss}$ distribution becomes more disperse.

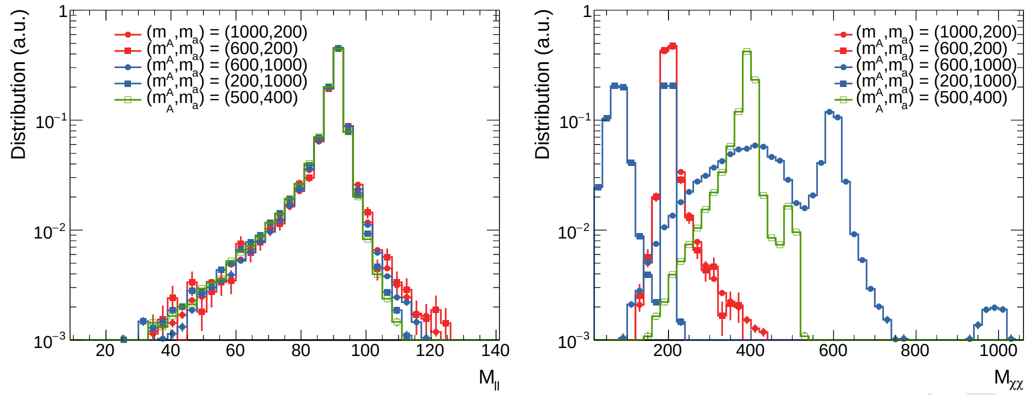

Figure 22: Distributions of the invariant mass of the dilepton (left) and $\chi\overline{\chi}$ systems (right) with no selection applied in addition to the generation cuts. The M_{ll} distribution is centered around the Z boson mass independent of the chosen parameter point, indicating that there is no contribtion from $\gamma*$ exchange. The $M_{\chi\overline{\chi}}$ distribution

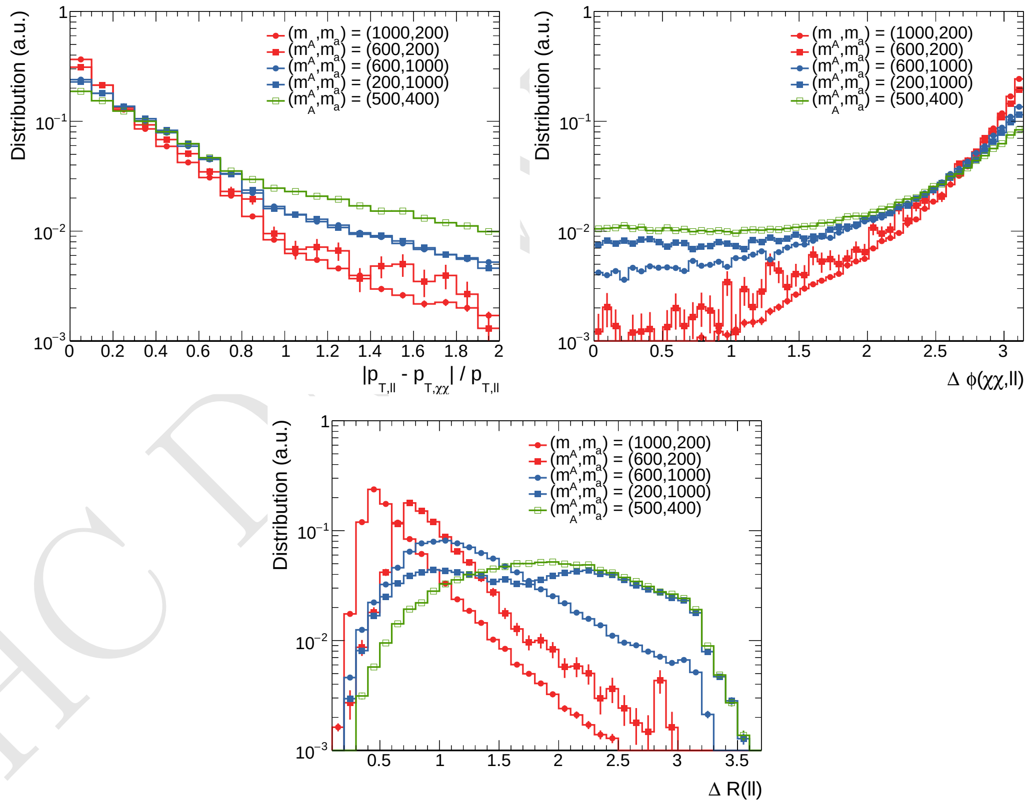

Figure 23: Distributions of the main selection variables after preselection: p_T balance (top panel), $\Delta\Phi$ (middle) and ΔR (bottom). The shown parameter points illustrate the different qualitative behavior in the three different mass regions.

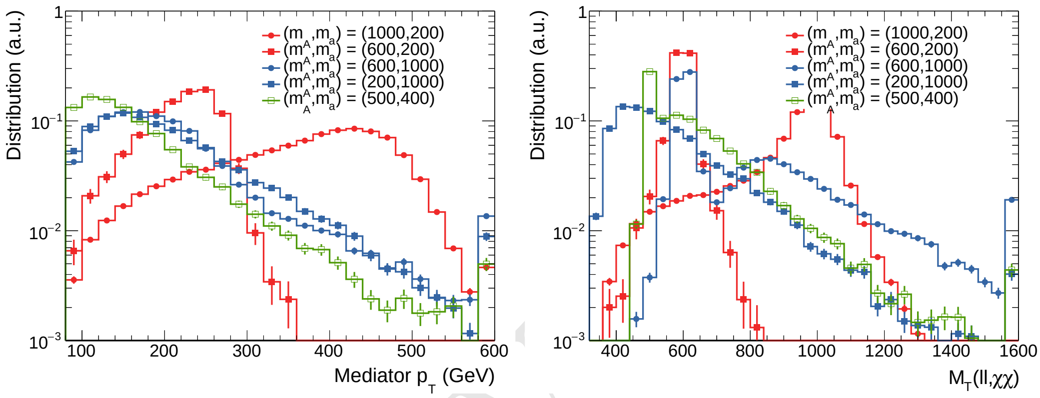

Figure 24: E_T^{miss} and MT distributions in the signal region. The E_T^{miss} distribution shows a Jacobian structure in the $M_A > M_a$ regime, the location of which strongly depends on M_A. In the region of inverted mass hierarchy $M_A < M_a$, the spectrum is less structured and does not fall off as steeply towards higher values. For a small mass splitting of $M_a - M_A \approx M_Z$, the spectrum is shifted to much lower values of E_T^{miss}. The MT distribution allows to access the resonant nature of the process. Clear mass peaks are present for the normal mass hierarchy. In the inverted region, the MT distribution is more sensitive to the mass difference $M_a - M_A$ than the E_T^{miss} distribution, allowing to differentiate between signal hypotheses that give near-identical E_T^{miss} distributions.

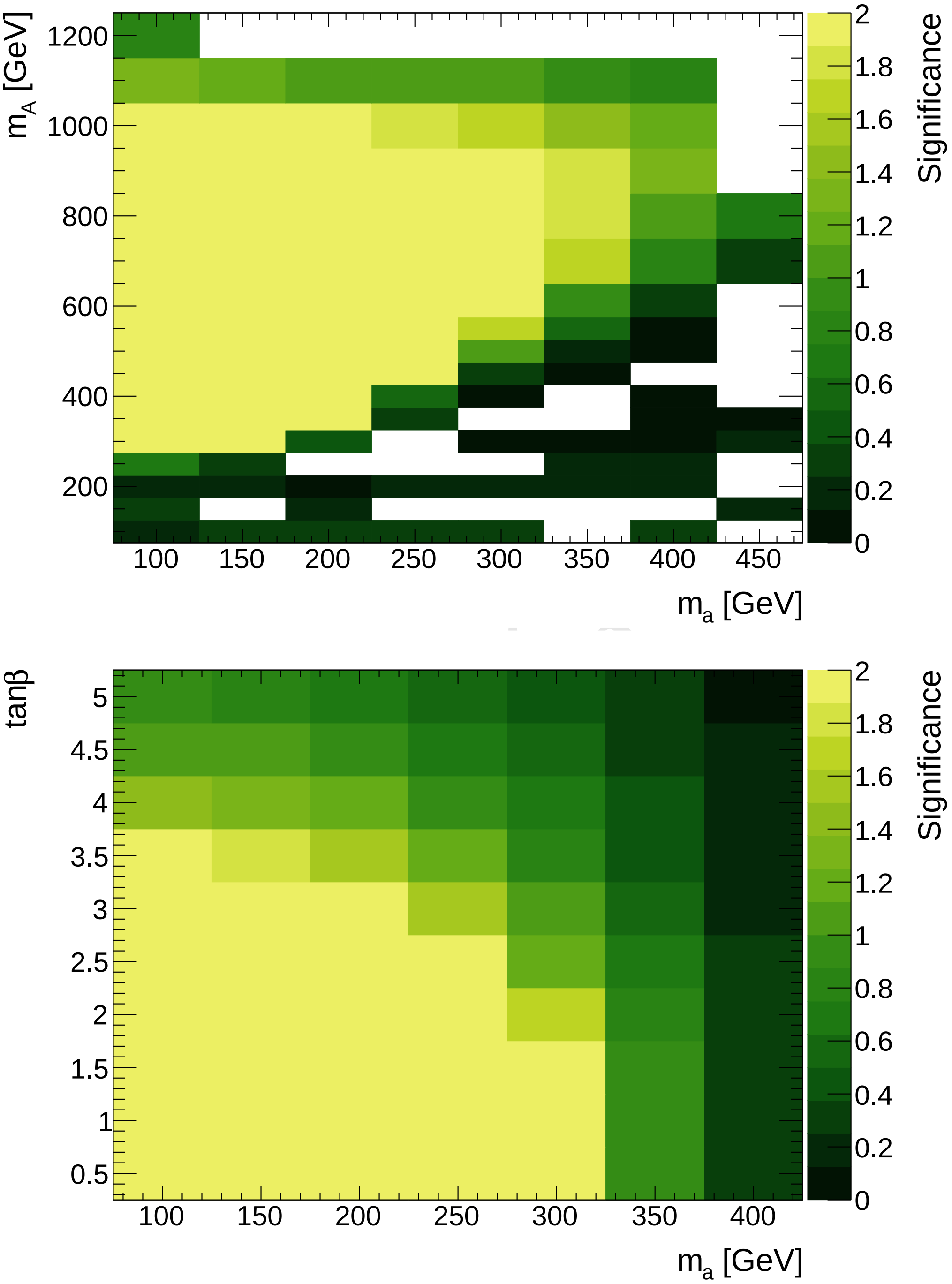

Figure 25: Expected significances are calculated using published background estimates and assuming a reconstruction efficiency of 75%. The LHC is expected to be sensitive to regions with significances greater than 2.

4.1.4 Studies of DM+heavy flavor signature

Heavy flavour final state have sizeable contributions to the production of the CP-even and CP-odd scalar mass eigenstates, due to the Yukawa structure of the couplings in the matter sector. In the following sections, the most important signatures involving either visible or invisible decays of the heavy Higgses are reviewed.

4.1.5 Scanning the parameter space

Scan of $\tan\beta$ and $\sin\theta$: In the limit of small $\tan\beta$ values, the couplings of h_3 (A) and h_4 (a) to down-type quarks are heavily suppressed irrespectively of the Yukawa assignment. At LO, $t\bar{t}+\chi\bar{\chi}$ associated production is mediated through either CP-odd weak eigenstate, A or a, though it is shown in Fig. 26 that $a \to \chi\bar{\chi}$ is the dominant production mode. Although the relative mediatior contribution is dependent on $\tan\beta$, observables such as E_T^{miss} and top quark p_T do not have a kinematic dependence on $\tan\beta$ as demonstrated in Fig. 27.

Mixing of the CP-odd weak eigenstates is achieved through the mixing angle, θ. As shown in Fig. 28, the A and a mass peaks are quite narrow for values where $\sin\theta$ approaches 1, and $a \to \chi\bar{\chi}$ is the dominant $\chi\bar{\chi}$ production mode. However, no kinematic dependence on $\sin\theta$ is observed in the E_T^{miss} and top quark p_T as shown in Fig. 29.

Scan of $\mathrm{M_a}$ and $\mathrm{M_A}$: While the relevant kinematic distributions display no dependence on the aforementioned mixing angles, the same does not hold true for the masses, $\mathrm{M_a}$ and $\mathrm{M_A}$. As shown in Fig. 30, the E_T^{miss}, and leading and trailing top quark p_T distributions broaden with increasing $\mathrm{M_a}$. Similarly, for values of $\mathrm{M_A} < \mathrm{M_a}$, as $\mathrm{M_A}$ increases, the kinematic distributions mentioned above also broaden, as shown in Fig. 31.

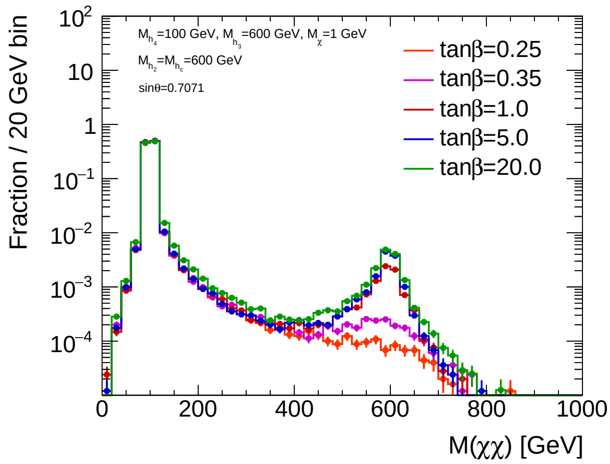

Figure 26: The mass distribution of the $\chi\bar{\chi}$ system for various values of $\tan\beta$, with $\mathrm{M_a} = 100$ GeV, $\mathrm{M_A} = 600$ GeV, $\mathrm{M_H} = \mathrm{M_{H\pm}} = 600$ GeV, and $\sin\theta = 0.7071$.

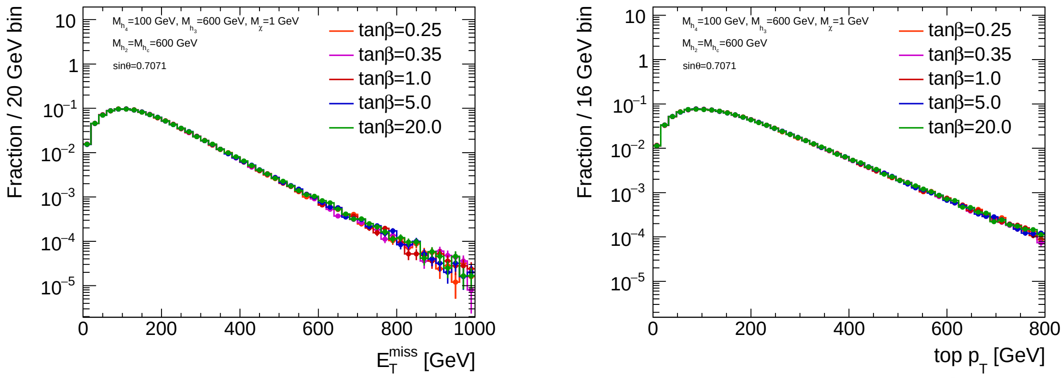

(a) E_T^{miss} (b) top p_T

Figure 27: The E_T^{miss} and top p_T distribution for inclusive $t\bar{t}+\chi\bar{\chi}$ production for various values of $\tan\beta$, with $\mathrm{M_a}$ = 100 GeV, $\mathrm{M_A}$ = 600 GeV, $\mathrm{M_H} = \mathrm{M_{H\pm}}$ = 600 GeV, and $\sin\theta = 0.7071$.

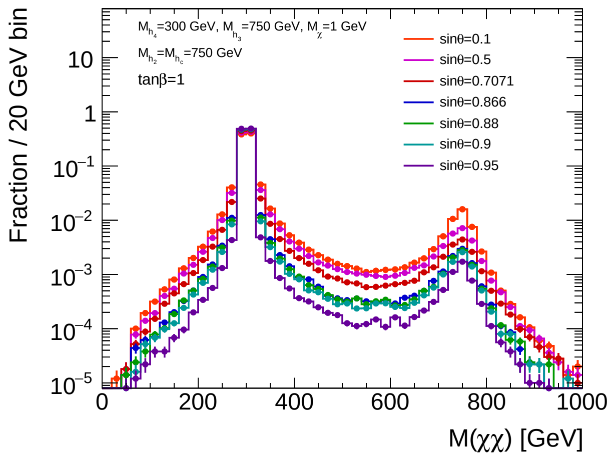

Figure 28: The mass distribution of the $\chi\bar{\chi}$ system for various values of $\sin\theta$, with $\mathrm{M_a}$ = 300 GeV, $\mathrm{M_A}$ = 750 GeV, $\mathrm{M_H} = \mathrm{M_{H\pm}}$ = 750 GeV, and $\tan\beta = 1$.

4.1.6 Comparison with DMsimp Pseudoscalar Model

To date, simplified models of DM (`DMsimp`) are used to interpret Run II CMS and ATLAS HF+DM searches. A comparison of the pertinent kinematic distributions between the pseudoscalar simplified model and the 2HDM+a model for the same value of $\mathrm{M_a}$ are shown in Fig. ??. The kinematics of the pseudoscalar `DMsimp` model with $\mathrm{M_a}$ = 100 GeV map directly onto those of the 2HDM+a model with $\mathrm{M_a}$ = 100 GeV, $\mathrm{M_A}$ = 600 GeV, $\mathrm{M_H} = \mathrm{M_{H\pm}}$ = 600 GeV, $\sin\theta = 0.7071$, and $\tan\beta = 1$. From the mass distribution of the $\chi\bar{\chi}$ shown in Fig. 33, it is evident that the 2HDM+a model contains contributions from both the light and heavy pseudoscalar mediator as in the `DMsimp` model.

In Fig. 34, relevant kinematic distributions, commonly employed in HF+DM searches,

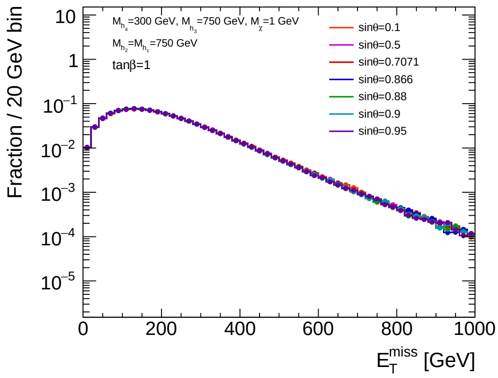

(a) E_T^{miss}

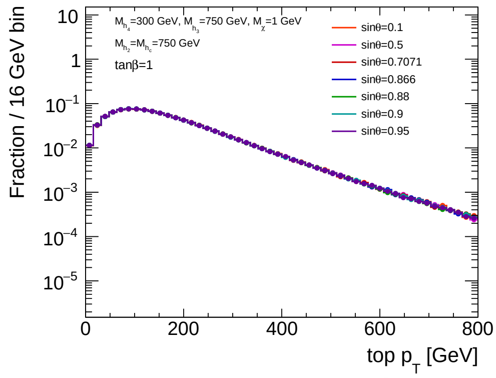

(b) top p_T

Figure 29: The E_T^{miss} and top p_T distribution for inclusive $t\bar{t} + \chi\bar{\chi}$ production for various values of $\sin\theta$, with $\mathrm{M_a} = 300$ GeV, $\mathrm{M_A} = 750$ GeV, $\mathrm{M_H} = \mathrm{M_{H^\pm}} = 750$ GeV, and $\tan\beta = 1$.

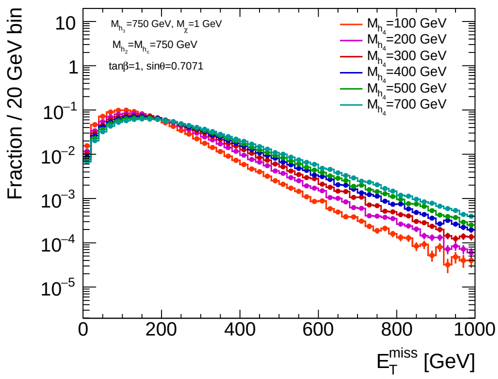

(a) E_T^{miss}

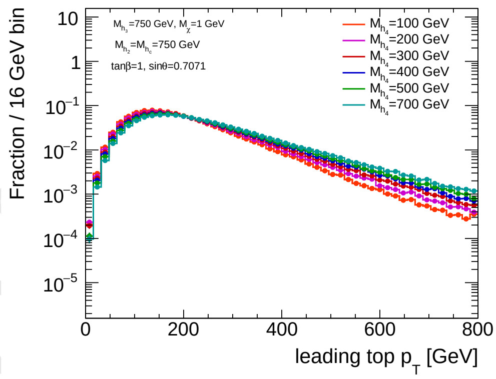

(b) Leading top p_T

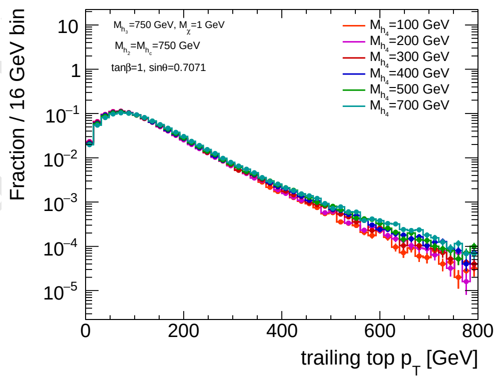

(c) Trailing top p_T

Figure 30: The E_T^{miss}, leading and trailing top p_T distributions for inclusive $t\bar{t} + \chi\bar{\chi}$ production for various values of $\mathrm{M_a}$, with $\mathrm{M_A} = 750$ GeV, $\mathrm{M_H} = \mathrm{M_{H^\pm}} = 750$ GeV, $\tan\beta = 1$, and $\sin\theta = 0.7071$.

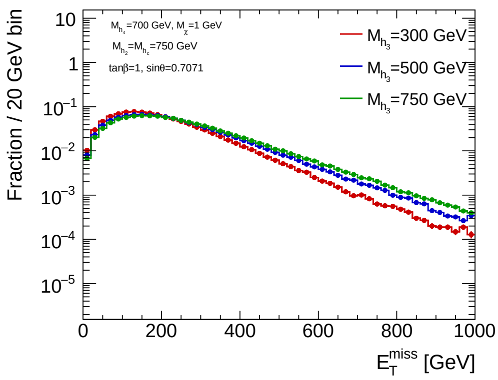

(a) E_T^{miss}

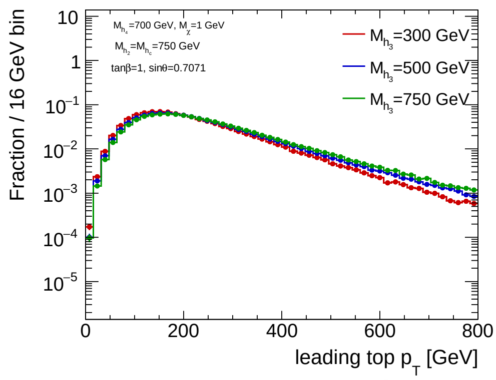

(b) Leading top p_T

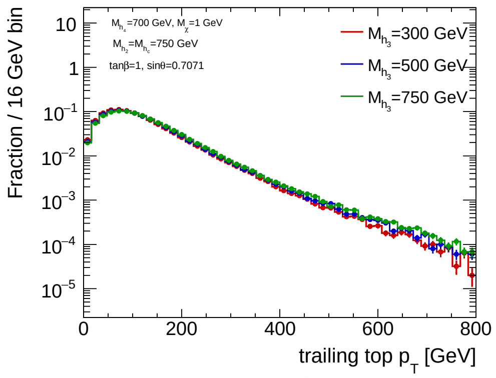

(c) Trailing top p_T

Figure 31: The E_T^{miss}, leading and trailing top p_T distributions for inclusive $t\bar{t} + \chi\bar{\chi}$ production for various values of $\mathrm{M_A}$, with $\mathrm{M_a} = 700$ GeV, $\mathrm{M_H} = \mathrm{M_{H^\pm}} = 750$ GeV, $\tan\beta = 1$, and $\sin\theta = 0.7071$.

are mapped from the `DMsimp` pseudoscalar models to the 2HDM+a model, with the mediator masses corresponding to the additional light pseudoscalar in the latter model. The dashed distributions represent the `DMsimp` model, while the solid are the 2HDM+a model distributions. The $t\bar{t} + \chi\bar{\chi}$ process was generated at LO precision using both models. As can be seen, the kinematics do not change appreciably between the models generated at the same value of $\mathrm{M_a}$. A discussion on cross-section rescaling procedures can be found in the following section.

4.1.7 Recasting existing tt+$E_T^{\rm miss}$ and bb+$E_T^{\rm miss}$ signatures

These two signatures are dominantly produced in diagrams involving the invisible decays of the two CP-odd scalars. Their relevance is therefore determined by the two pseudoscalar masses, $m(A)$ and $m(a)$ and it is a function of $sin\theta$ and $tan\beta$. For both bb and tt associated productions, we find that the highest sensitivity of this signatures is obtained for high values of $sin\theta$.

The 2HDM+a model is equivalent to a single pseudoscalar simplified model (DMF)

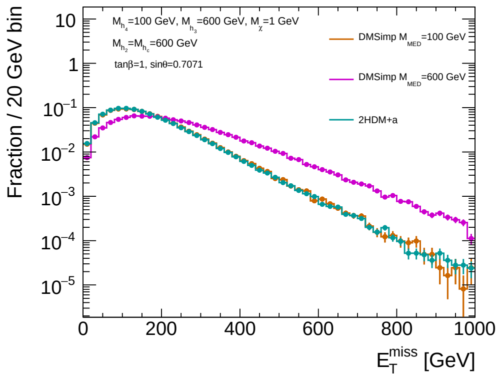

(a) E_T^{miss}

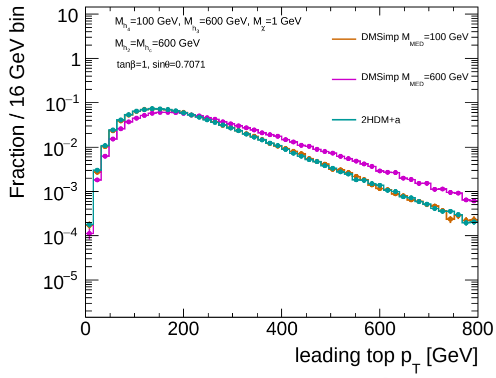

(b) Leading top p_T

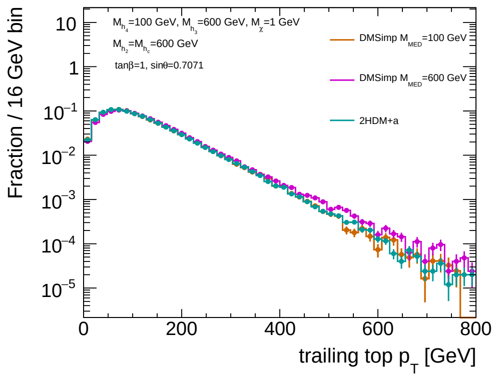

(c) Trailing top p_T

Figure 32: The E_T^{miss}, leading and trailing top p_T distributions for inclusive $t\bar{t}+\chi\bar{\chi}$ production for various values of $\mathrm{M_A}$, with $\mathrm{M_a} = 700$ GeV, $\mathrm{M_H} = \mathrm{M_{H^\pm}} = 750$ GeV, $\tan\beta = 1$, and $\sin\theta = 0.7071$.

when A is much heavier than a, and therefore the former does not contribute to the considered final state. However, when the two mediators are closer in mass, the $pp \to ttA$ contribution becomes more relevant as it is possible to observe in Figure 35, where the two models are compared assuming $m(A) = 750$ GeV and two different values for $m(a)$. An excellent agreement was observed between $DMSIMP$ and $2HDMp$ on parton-level variables sensitive to the helicity structure of the interaction between top and the mediator[**?**], if the invariant mass of the two DM particles in the 2HDM is required to be smalle than 200(300) GeV for $m(a) = 150(300)$ GeV respectively, giving confidence that, once the contribution from A production is separated, it is possible to fully map the $2HDM + a$ kinematics into the DMF simplified model.

This remapping is achieved by taking for each set of the parameters the average of the selection acceptances for $m(A)$ and $M(A)$ as calculated with $DMSIMP$ weighted by the respective cross-section for A (σ_A) and a (σ_a) production, in formulas

$$Acc_{2HDM}(m(A), M(a)) = \frac{\sigma_a \times Acc_{DMSIMP}(m(a)) + \sigma_A \times Acc_{DMSIMP}(m(A))}{\sigma_a + \sigma_A} \quad (4.7)$$

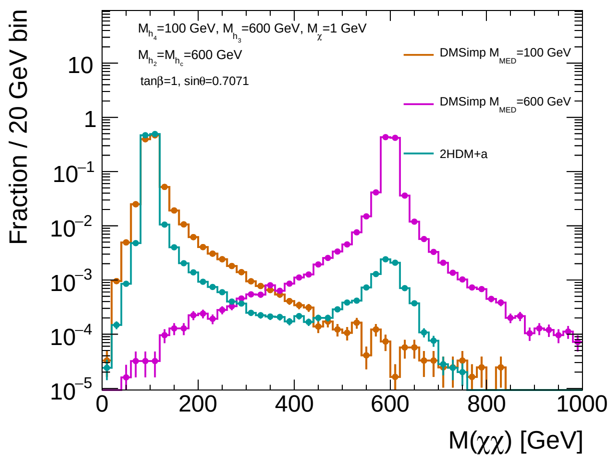

Figure 33: The mass distribution of the $\chi\bar{\chi}$ system for `DMsimp` pseudoscalar models with $\mathrm{M_a}$ = 100 GeV and $\mathrm{M_a}$ = 600 GeV, compared with 2HDM+a with $\mathrm{M_a}$ = 100 GeV, $\mathrm{M_A}$ = 600 GeV, $\mathrm{M_H} = \mathrm{M_{H^\pm}}$ = 600 GeV, $\sin\theta = 0.7071$ and $\tan\beta = 1$.

The acceptance in this case is a parton level implementation of the two-lepton analysis described in [arXiv:1710.11412]. The acceptance estimated in this way is shown as red triangles in Figure 36, and an excellent agreement can be seen with the acceptances evaluated directly on the 2HDM samples. The acceptance estimated in this way is shown as red triangles in Figure 36, and an excellent agreement can be seen with the acceptances evaluated directly on the 2HDM samples. Further validation were performed also on the acceptances calculated for zero and one lepton final states [1710.11412,1711.11520], both as a function of $sin\theta$ and $tan\beta$ and can be observed in Fig 37. Finally, the formula was succesfully tested also the situation in which $|m(A) - m(a)| \sim 50$ GeV, implying the possibility of a large interference between the production of the two bosons.

4.1.8 Flavour scheme recommendations and studies

The relevant kinematic distributions for $t\bar{t} + \chi\bar{\chi}$ associated production in the context of this model are shown to be independent from the choice of PDF flavour scheme. In Figures 38–40, the E_T^{miss}, which is taken to be the p_T of the $\chi\bar{\chi}$ system, and the p_T distribution of the top quarks is presented using the 4 and 5-flavour scheme. The 4-flavour LHAPDF ID is 263400 and corresponds to `NNPDF30_lo_as_0130_nf_4`, and the 5-flavour LHAPDF ID is 263000 and corresponds to `NNPDF30_lo_as_0130`. As demonstrated for various configurations of the 2HDM+a model parameters, the kinematics are not affected by the flavour scheme choice of PDF. Furthermore, the difference in cross-section between the 4-flavour and 5-flavour generated LO $t\bar{t} + \chi\bar{\chi}$ process is at the $2-3\%$ level, as noted in Tab. 2.

Despite the lack of kinematic dependence on flavour scheme, it is recommended to use the 5-flavour PDF.Add support/discussion and references

Motivations for an high $tan\beta$ scan for bb+$E_T^{\rm miss}$ The projection of sensitivity in $tan\beta$ for benchmark #2, based on the CMS results for bb+MET [arXiv:1706.02581] are

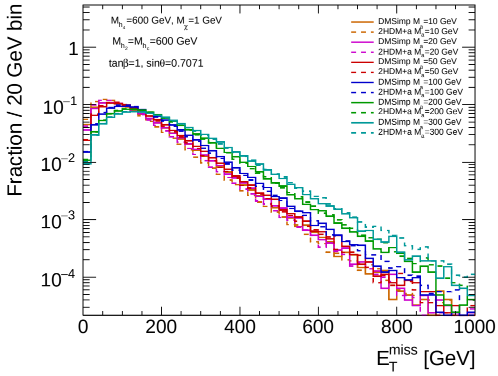

(a) E_T^{miss}

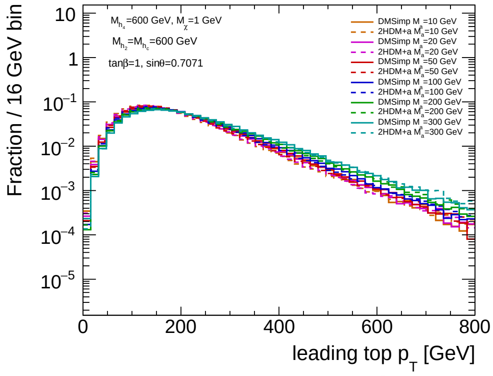

(b) Leading top p_T

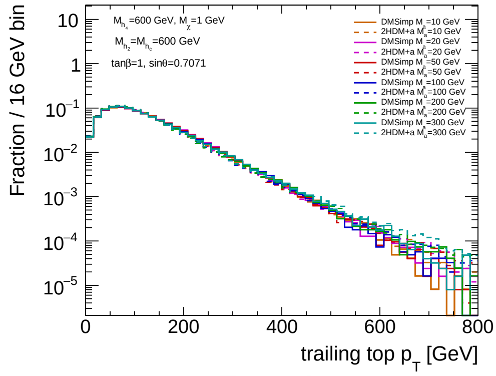

(c) Trailing top p_T

Figure 34: The E_T^{miss}, leading and trailing top p_T distributions for inclusive $t\bar{t} + \chi\bar{\chi}$ production generated from the `DMsimp` (solid) and the 2HDM+a (dashed) models with various values of $\mathrm{M_a}$. The 2HDM+a models are generated with the following model parameters:$\mathrm{M_A} = 600$ GeV, $\mathrm{M_H} = \mathrm{M_{H\pm}} = 600$ GeV, $\tan\beta = 1$, and $\sin\theta = 0.7071$.

$\mathrm{M_{h_2}, M_{h_c}}$ [GeV]	$\mathrm{M_{h_3}}$ [GeV]	$\mathrm{M_{h_4}}$ [GeV]	$\sin\theta$	$\tan\beta$	4F σ (pb)	5F σ (pb)
750	500	100	0.7071	1	0.0988596	0.0964933
750	750	200	0.7071	1	0.0445115	0.043149
750	300	200	0.25	1	0.0310152	0.0300196

Table 2: Configurations of the 2HDM+a model used to generate the $t\bar{t} + \chi\bar{\chi}$ process at LO and the corresponding cross-sections from the 4-flavour (4F) and 5-flavour (5F) PDF.

shown in Figure 41. The reach for an upper bound on tan(beta) with bb+MET shows good potential, for $tan\beta$ values above 10.

Say something about high width for H?

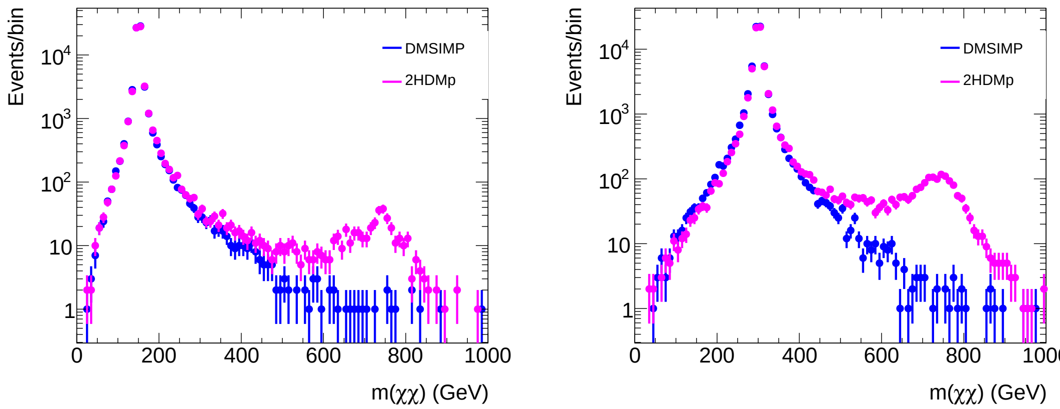

Figure 35: Comparison of $m(\chi\chi)$, the invariant mass of the two DM particles for the $DMSIMP$ (blue) and the $2HDMp$ model (magenta). The plot on the left (right) shows the comparison for $m(a) = 150(300)$ GeV respectively.

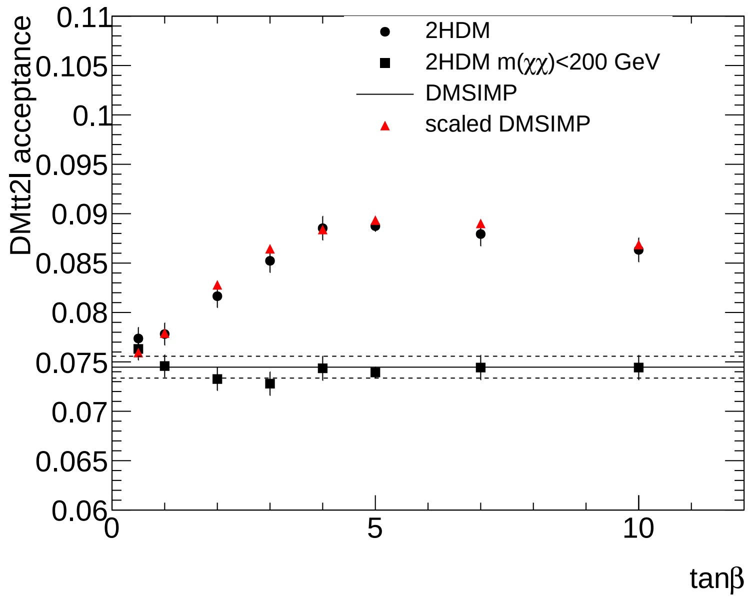

Figure 36: Acceptance of the two-lepton analysis as a function of $\tan\beta$ for the $2HDMp$ model (round markers), for the $2HDMp$ model considering only events with $m(\chi\chi) <$ 200 GeV (square markers), and for the $DMSIMP$ model (full line) for a mediator mass of 150 GeV. The two dashed lines indicate the statistical error of the $DMSIMP$. The value of $m(A)$ is fixed at 600 GeV, and $\sin\theta = 0.35$. The acceptance calculated from the $DMSIMP$ acceptance rescaled following the prescription 4.7 (red triangles) is also shown.

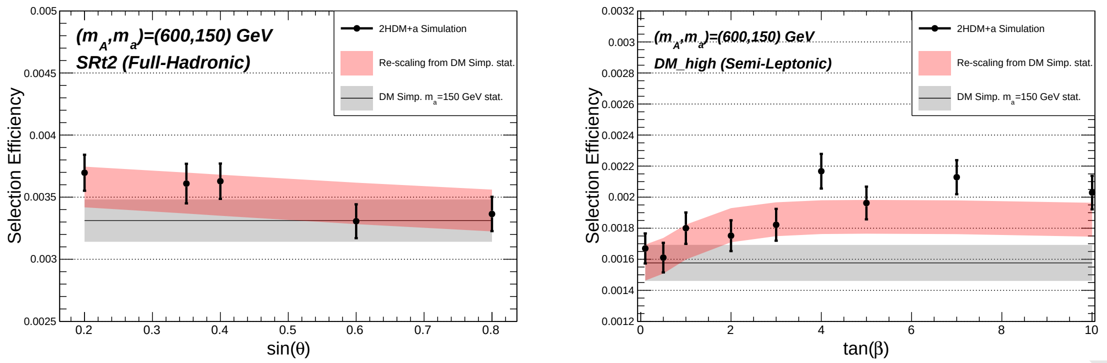

Figure 37: Validation of the re-scaling formula on zero and one lepton final states as a function of $tan\beta$ and $sin\theta$ parameters

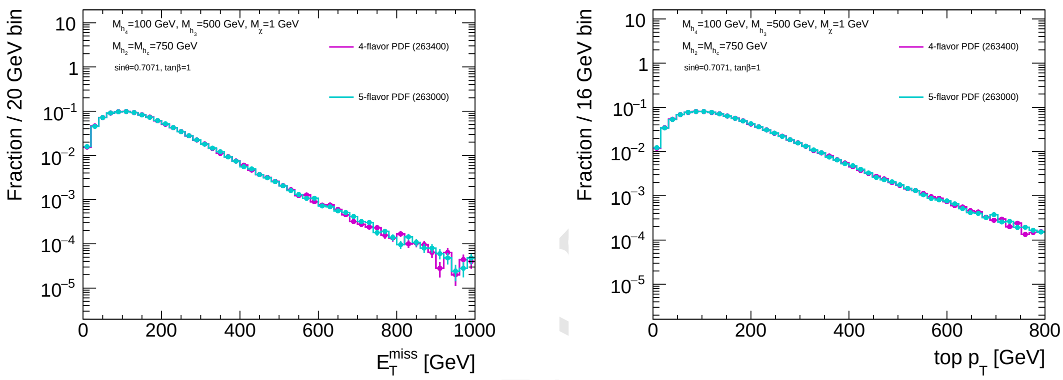

(a) E_T^{miss} (b) top p_T

Figure 38: E_T^{miss} and top p_T distributions for $M_{h_4} = 100$ GeV, $M_{h_3} = 500$ GeV, $M_{DM} = 1$ GeV, $\sin\theta = 0.7071$, and $\tan\beta = 1$.

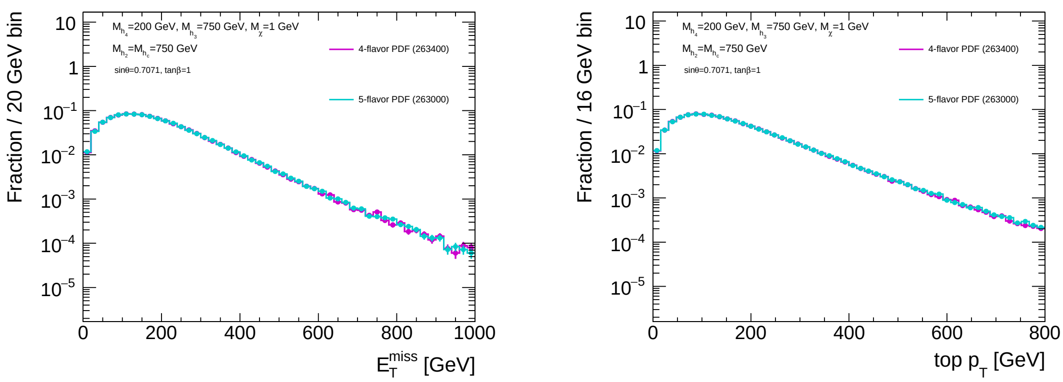

(a) E_T^{miss} (b) top p_T

Figure 39: E_T^{miss} and top p_T distributions for $M_{h_4} = 200$ GeV, $M_{h_3} = 750$ GeV, $M_{DM} = 1$ GeV, $\sin\theta = 0.7071$, and $\tan\beta = 1$.

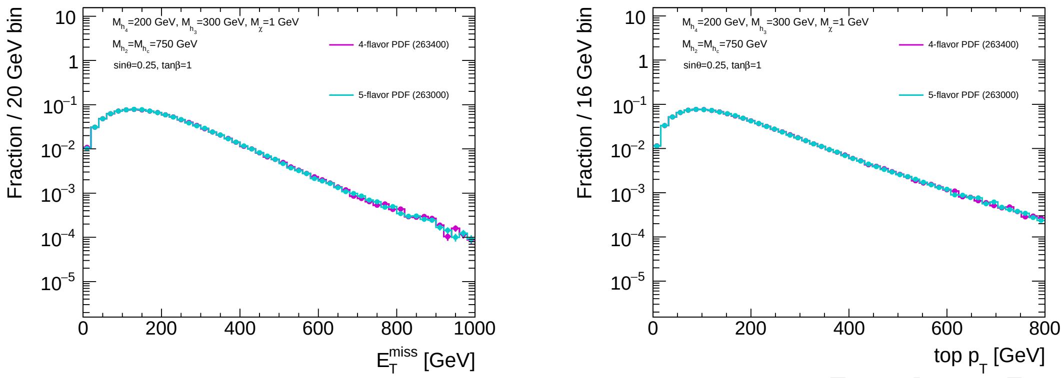

(a) E_T^{miss} (b) top p_T

Figure 40: E_T^{miss} and top p_T distributions for $M_{h_4} = 200$ GeV, $M_{h_3} = 300$ GeV, $M_{DM} = 1$ GeV, sin$\theta = 0.25$, and tan$\beta = 1$.

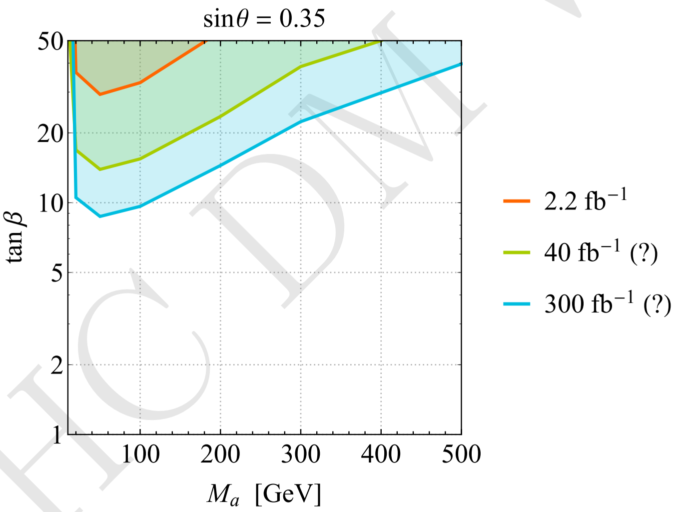

Figure 41: Sensitivity projection for benchmark #2 based on the CMS results for bb+MET [arXiv:1706.02581].

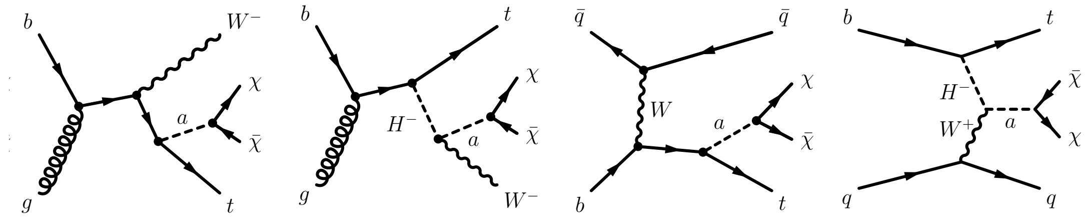

(a) (b) (c) (d)

Figure 42: Representative diagrams for tW and t-channel production of DM in association with a single top quark.

4.1.9 Motivation for a dedicated tW+E_T^{miss} search

The sensitivity of the LHC experiments to the associated production of dark matter with a single top has been recently studied [**?**] in the framework of an extension of the standard model featuring two Higgs doublets and an additional pseudoscalar mediator. This study extends the work of previous literature [**?**], which demostrated using a simplified model that the consideration of final states involving a single top quark and DM (DMt) increases the coverage of existing analyses targeting the DM$t\bar{t}$ process.

Like single top production within the SM, the DMt signature in the model receives three different types of contributions at leading order (LO) in QCD. These are t-channel production, s-channel production and associated production together with a W boson (tW) (Fig. 42). When the decay $H^{\pm} \to W^{\pm}a$ is possible, the $H^{\pm}$ is produced on-shell, and the cross-section of $pp \to tW\chi\chi$, assuming $H^{\pm}$ masses of a few hundred GeV, is around one order of magnitude larger than the one for the same process in the simplified model. Moreover the production and cascade decay of a resonance yields kinematic signatures which can be exploited to separate the signal from the SM background.

Dedicated selections considering one and two lepton final states are developed to assess the coverage in parameter space for this signature at a centre-of-mass energy of 14 TeV assuming an integrated luminosity of 300 fb^{-1} in Ref. [**?**]. Background and signal Monte Carlo simulated samples are employed for the estimate of the results. The effect of the detector on the kinematic quantities utilised in the analysis is simulated by applying a Gaussian smearing to the momenta of the different reconstructed objects and reconstruction and tagging efficiency factors. Figure 43 shows the sensitivy reach for two of the parameter scans proposed in this whitepaper. On the top panel the exclusion reach for the $m(a), tan\beta$ plane is presented, assuming $sin\theta = 0.35$ and $m(A) = m(H^{\pm}) = m(H) = 500$ GeV. It is possible to observe that for this scenario the sensitivity reach is comparable to the one from the mono-h signature as presented in Ref. [1]. On the bottom panel of Figure 43 the signature's sensitivity to benchmark #4 is evaluated for the first time.

4.1.10 Uncovered signatures with $tth + E_T^{\text{miss}}$

As discussed in Section **??**, the production of the heavy mediator A gives a sizeable contribution to the $tt + E_T^{\text{miss}}$ production cross section in the $2HDM + a$ model. This is also

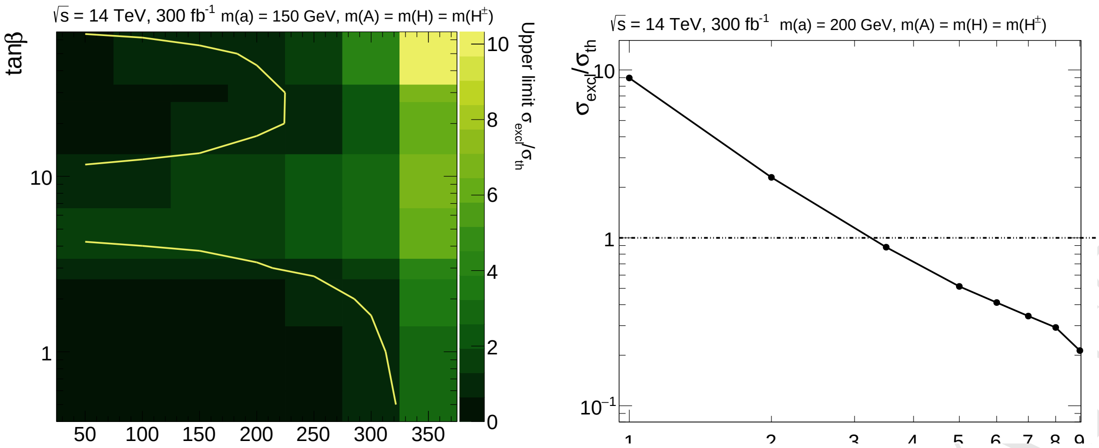

Figure 43: Exclusion reach for benchmark #2 (top) and benchmark #4 (bottom), assuming $sin\theta = 0.35$ and $m(A) = m(H^{\pm}) = m(H) = 500$ GeV.

true for the heavy H. When the decay of these mediators into the lightest pseudoscalar a is allowed, this decay process dominates over the direct decay into $\chi\chi$. In symmetry with what happens for the mono-h signature discussed in [1], for certain region of parameter space the signatures $pp \to t\bar{t}A \to t\bar{t}ah$ and $pp \to t\bar{t}H \to t\bar{t}aZ$ become sizeable. For the former case, it can be estimated from Fig. 12(b) of Ref. [1] that for relatively small $m(A)$ the $pp \to t\bar{t}ah$ cross section can be up to 30% that of the $pp \to t\bar{t}\chi\chi$ process. The interplay between the parameters of the model, and especially between the heavy higgs masses for these types of final state render the phenomenology interesting and variegated, as can be seen for example in the branching ratio study of Fig. 44, although further studies are needed to fully understand the interplay and the complementarity between these $tth+E_T^{\mathrm{miss}}$ channels and the traditional heavy flavour dark matter searches.

4.1.11 Top pair resonant searches

Heavy scalar and pseudoscalar bosons decaying dominantly into top-quark pairs can be searched for by studying the resulting $\bar{t}t$ invariant mass spectra. However, interference effects between the signal processes and the SM $\bar{t}t$ production distort the signal shape from a single peak to a peak-dip structure [appropriate REFs?]. Interference between a loop-induced and a tree-level process cannot currently be simulated in MadGraph. To amend this problem, the "Higgs_Effective_Couplings_FormFactor" approach [**?**] is implemented in the UFO, replacing the loop production by an effective vertex. **Are we interested to insert one of the validation plots from atlas?**

4.1.12 Four tops final states

Work in progress

4.1.13 Final proposal for parameter scan

- a two-dimensional scan in the light pseudoscalar mass (ma) - heavy pseudoscalar mass (mA) plane where ma = mA, fixing tanBeta to 1.0, sinTheta to 0.35 and the

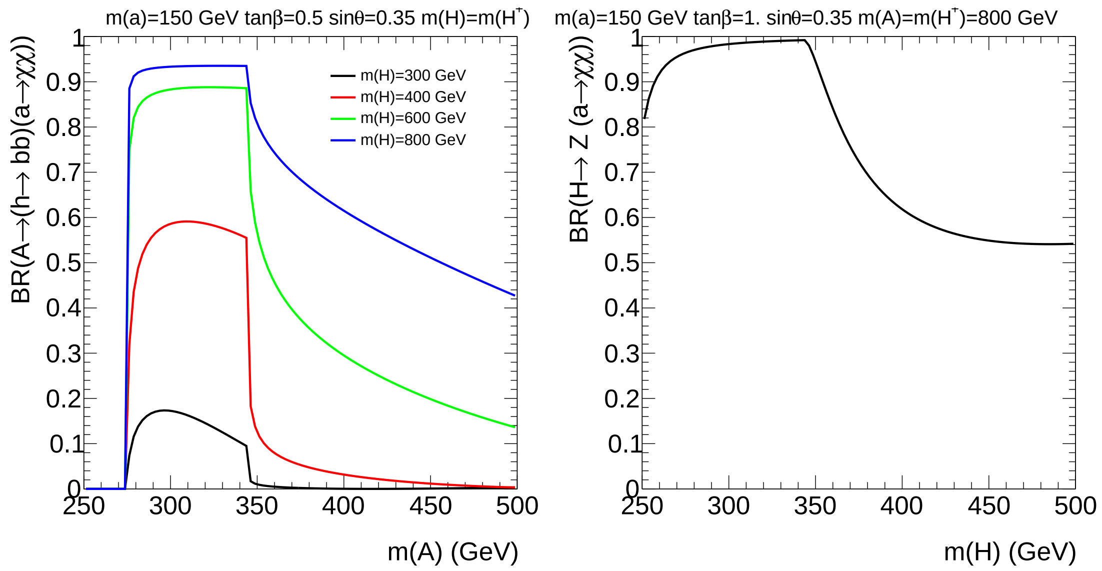

Figure 44: Example of the dependence of the A and H branching ratio into ah as a function of some parameters of the 2HDM model.

Dark Matter mass (mDM) to 10 GeV.

- a one-dimensional scan in DM mass from 1 GeV to 500 GeV for a point in the middle of the sensitivity range for the mono-V analyses at mA=600, ma=250 GeV, so the connection between this model and cosmology is clear as the measured relic density starts being satisfied at values of DM mass around 100 GeV

In order to explore changes in complementarity with different analyses and kinematics, this should be complemented by:

- a two-dimensional scan in the ma tanBeta plane, for comparison with the ttbar+MET / bbar+MET analyses. In this case, the charged Higgs mass (mH+/-), the heavy pseudoscalar mass (mA) and the heavy Higgs mass (mH) should be fixed to 600 GeV. This scan includes points: 50, 45, 40, 35, 30, 25, 20, 15, 10, 5 for M(a) masses between 10 and 350 GeV. The high-tanBeta points would be of primary interest to the HF + DM searches. Uli's studies have shown that one can simply reweight the existing tt+DM/bb+DM models from DMF to the new 2HDM+PS cross sections; full simulation of the newly proposed 2HDM+PS points is not required.

- two one-dimensional scans in sin_θ for the comparison of mono-Higgs and bbar+MET analysis (it is expected that the bbar+MET analysis will only have to rescale previous models/cross-sections) [2]: - mH = mA = mH = 600GeV , ma = 200GeV, tanBeta=1 - mH = mA = mH = 1000GeV , ma = 350GeV, tanBeta=1

The PDF recommended is five-flavor. ATLAS will use the NNPDF3.0 PDF set. Some text by Fabio Maltoni and Ulrich Haisch can be found in the texinputs_app folder.

5 Connection with cosmology

An important requirement for models of dark matter is their consistency with existing astrophysical observations, namely the observed dark matter relic density. The relic density is driven by the annihilation cross-section of dark matter into SM particles. For a given model of dark matter-SM interactions, the annihilation cross-section is fully defined and a calculation of the resulting relic density can be performed.

5.1 Technical setup

The MadDM [19, 20] plugin for MG5_aMC@NLO is used to calculate the present-day relic density for this model. By modeling the thermal evolution of the cross-section during the expansion of the early universe, the time of freeze-out is determined. All tree-level annihilation processes are taken into account, and the Yukawa couplings of all fermions are taken to be non-zero. The Feynman diagrams of annihilation processes taken into account in this calculation are shown in Fig. 45. Generally, the annihilation proceeds via single or double s-channel exchange of the pseudoscalars a and A, with subsequent decays. Since MadDM uses only tree-level diagrams, contributions from off-shell pseudoscalars can only be taken into account for the case of single s-channel mediation with direct decay of the pseudoscalar to SM fermions. If the pseudoscalar instead decays to other bosons or if the annihilation proceeds through double s-channel diagrams, the outgoing bosons are taken to be on-shell and their decays are not simulated.

In all scans presented here, the common parameter choices $sin(\theta) = 0.35$, $m_h = 125GeV$, $g_\chi = 1$, $\lambda_i = 3$ are used.

5.2 Results

The relic density is shown for a scan in the M_a-M_χ plane in Fig. 46. For small values of M_χ below the mass of the top quark, DM is mostly overabundant. In this regime, annihilation to quarks is suppressed by the small Yukawa couplings of the light fermions. The observed relic density can only be achieved for $M_\chi \approx M_a/2$, where annihilation is resonantly enhanced, or for $M_\chi \approx (M_a + M_h)/2$, close to the threshold for the $\chi\chi \to ha$ process. Above the top threshold, annihilation into fermions becomes very efficient and DM is underabundant. As M_χ increases further, annihilation via single s-channel diagrams is increasingly suppressed and the relic density rises again. The observed density is reproduced again for $M_\chi \approx 1\text{TeV}$ at low M_a. For values of M_a beyond the LHC reach of a few TeV, the allowed parameter region at the top threshold $M_\chi \approx m_{\text{top}}$ stays independent of the value of M_a, indicating that a DM candidate that is mass degenerate with the top quark cannot be excluded by LHC searches alone.

The dependence of the relic density on the choice of M_χ is further explored by performing a one-dimensional scan, as shown in Fig. 47. The relic density shows clear structures corresponding to the previously discussed regions of resonant enhancement, as well as kinematic boundaries. Overall, the behavior is dominated by the low-M_χ suppression of the annihilation cross-section, the reosnant enhancement at $M_\chi = M_a/2$ and the kinematic top thresholds. Other effects, such as resonant enhancement of $\chi\chi \to A$ annihilation are present, but only have small effects.

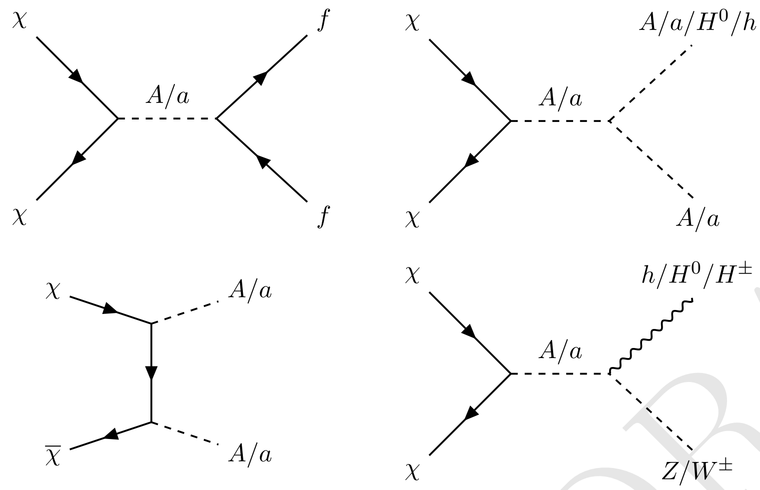

Figure 45: Annihilation diagrams taken into account in the relic density calculation.

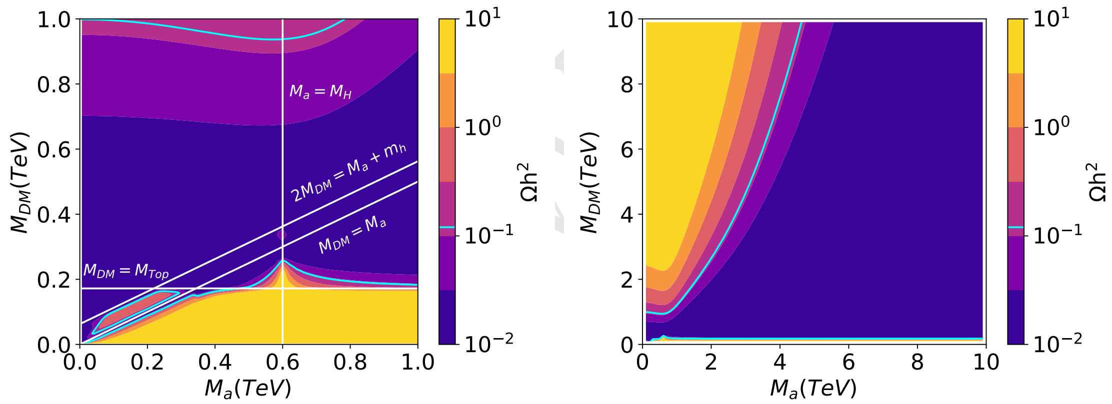

Figure 46: Predicted relic density for a two-dimensional scan of M_χ and M_a. The other parameters of the model remain fixed with $m_H = m_A = m_{H^\pm} = 600\,\text{GeV}$ and $\tan\beta = 1$, as well as the default choices described in the text. The color scale indicates the relic density, the cyan solid line shows the observed value of $\Omega h^2 = 0.12$. The color scale is truncated at its ends, i.e. values larger than the maximum or smaller than the minimum are shown in the same color as the maximum/minimum. While the left focuses on the mass region relevant to collider searches, the right panel shows the development of the relic density for a larger mass region.

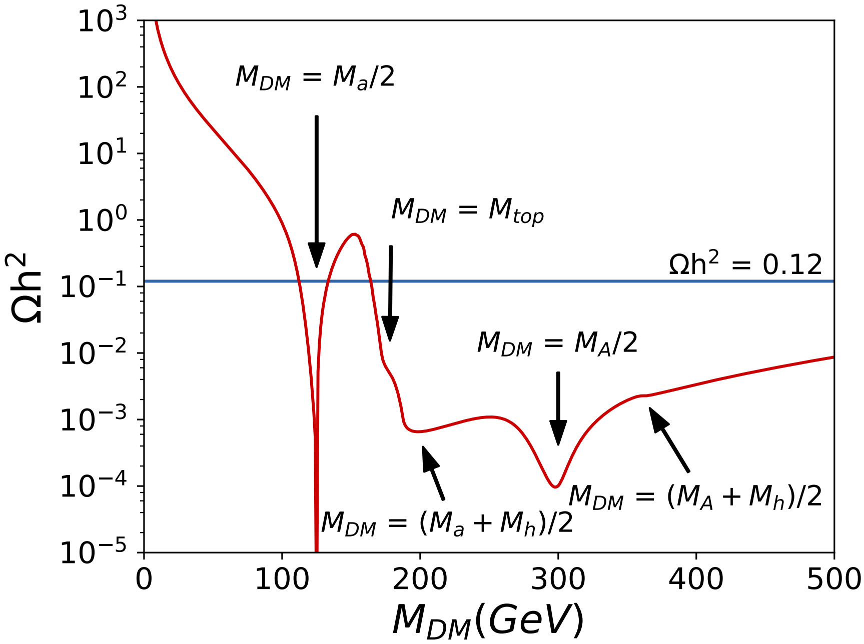

Figure 47: Relic density for a one-dimensional scan of M_χ. The other parameters of the model remain fixed with $m_H = m_A = m_{H^\pm} = 600\,\text{GeV}$, $M_a = 250\,\text{GeV}$ and $\tan\beta = 1$, as well as the default choices described in the text. Various kinematic thresholds and regions of resonant enhancement are visible. Consistency with the observed value of $\Omega h^2 = 0.12$ is mainly controlled by the resonant enhancement of $\chi\chi \to a$, as well as the onset of $\chi\chi \to t\bar{t}$.

6 Conclusions

References

[1] M. Bauer, U. Haisch, and F. Kahlhoefer, *Simplified dark matter models with two Higgs doublets: I. Pseudoscalar mediators*, *JHEP* **05** (2017) 138, [arXiv:1701.07427].

[2] N. F. Bell, G. Busoni, and I. W. Sanderson, *Self-consistent Dark Matter Simplified Models with an s-channel scalar mediator*, *JCAP* **1703** (2017), no. 03 015, [arXiv:1612.03475].

[3] S. Ipek, D. McKeen, and A. E. Nelson, *A Renormalizable Model for the Galactic Center Gamma Ray Excess from Dark Matter Annihilation*, *Phys. Rev.* **D90** (2014), no. 5 055021, [arXiv:1404.3716].

[4] J. M. No, *Looking through the pseudoscalar portal into dark matter: Novel mono-Higgs and mono-Z signatures at the LHC*, *Phys. Rev.* **D93** (2016), no. 3 031701, [arXiv:1509.01110].

[5] D. Goncalves, P. A. N. Machado, and J. M. No, *Simplified Models for Dark Matter Face their Consistent Completions*, *Phys. Rev.* **D95** (2017), no. 5 055027, [arXiv:1611.04593].

[6] J. F. Gunion and H. E. Haber, *The CP conserving two Higgs doublet model: The Approach to the decoupling limit*, *Phys. Rev.* **D67** (2003) 075019, [hep-ph/0207010].

[7] I. F. Ginzburg and I. P. Ivanov, *Tree-level unitarity constraints in the most general 2HDM*, *Phys. Rev.* **D72** (2005) 115010, [hep-ph/0508020].

[8] B. Grinstein, C. W. Murphy, and P. Uttayarat, *One-loop corrections to the perturbative unitarity bounds in the CP-conserving two-Higgs doublet model with a softly broken* $\mathbb{Z}_2$ *symmetry*, *JHEP* **06** (2016) 070, [arXiv:1512.04567].

[9] A. Barroso, P. M. Ferreira, I. P. Ivanov, and R. Santos, *Metastability bounds on the two Higgs doublet model*, *JHEP* **06** (2013) 045, [arXiv:1303.5098].

[10] F. Staub, *Reopen parameter regions in Two-Higgs Doublet Models*, arXiv:1705.03677.

[11] J. Alwall, R. Frederix, S. Frixione, V. Hirschi, F. Maltoni, O. Mattelaer, H. S. Shao, T. Stelzer, P. Torrielli, and M. Zaro, *The automated computation of tree-level and next-to-leading order differential cross sections, and their matching to parton shower simulations*, *JHEP* **07** (2014) 079, [arXiv:1405.0301].

[12] C. Degrande, C. Duhr, B. Fuks, D. Grellscheid, O. Mattelaer, and T. Reiter, *UFO - The Universal FeynRules Output*, *Comput. Phys. Commun.* **183** (2012) 1201–1214, [arXiv:1108.2040].

[13] **NNPDF** Collaboration, R. D. Ball et al., *Parton distributions for the LHC Run II*, *JHEP* **04** (2015) 040, [arXiv:1410.8849].

[14] **ATLAS** Collaboration, *Search for Dark Matter Produced in Association with a Higgs Boson Decaying to* $b\bar{b}$ *using 36* fb^{-1} *of pp collisions at* $\sqrt{s} = 13$ *TeV with the ATLAS Detector*, *Phys. Rev. Lett.* **119** (2017), no. 18 181804, [arXiv:1707.01302].

[15] **ATLAS** Collaboration, M. Aaboud et al., *Search for an invisibly decaying Higgs boson or dark matter candidates produced in association with a Z boson in pp collisions at* $\sqrt{s} = 13$ *TeV with the ATLAS detector*, *Phys. Lett.* **B776** (2018) 318–337, [arXiv:1708.09624].

[16] **CMS** Collaboration, A. M. Sirunyan et al., *Search for new physics in events with a leptonically decaying Z boson and a large transverse momentum imbalance in proton-proton collisions at* $\sqrt{s} = 13$ *TeV*, arXiv:1711.00431.

[17] G. Cowan, K. Cranmer, E. Gross, and O. Vitells, *Asymptotic formulae for likelihood-based tests of new physics*, *Eur. Phys. J.* **C71** (2011) 1554, [arXiv:1007.1727]. [Erratum: Eur. Phys. J.C73,2501(2013)].

[18] G. Cowan, *Discovery sensitivity for a counting experiment with background uncertainty*, tech. rep., Royal Holloway, London, (2012). Available [online] http://www.pp.rhul.ac.uk/~cowan/stat/medsig/medsigNote.pdf.

[19] M. Backovic, K. Kong, and M. McCaskey, *MadDM v.1.0: Computation of Dark Matter Relic Abundance Using MadGraph5*, *Physics of the Dark Universe* **5-6** (2014) 18–28, [arXiv:1308.4955].

[20] M. Backovic, A. Martini, O. Mattelaer, K. Kong, and G. Mohlabeng, *Direct Detection of Dark Matter with MadDM v.2.0*, *Phys. Dark Univ.* **9-10** (2015) 37–50, [arXiv:1505.04190].

References

[1] M. Bauer, U. Haisch, and F. Kahlhoefer, *Simplified dark matter models with two Higgs doublets: I. Pseudoscalar mediators*, *JHEP* **05** (2017) 138, [arXiv:1701.07427].

[2] N. F. Bell, G. Busoni, and I. W. Sanderson, *Self-consistent Dark Matter Simplified Models with an s-channel scalar mediator*, *JCAP* **1703** (2017), no. 03 015, [arXiv:1612.03475].

[3] S. Ipek, D. McKeen, and A. E. Nelson, *A Renormalizable Model for the Galactic Center Gamma Ray Excess from Dark Matter Annihilation*, *Phys. Rev.* **D90** (2014), no. 5 055021, [arXiv:1404.3716].

[4] J. M. No, *Looking through the pseudoscalar portal into dark matter: Novel mono-Higgs and mono-Z signatures at the LHC*, *Phys. Rev.* **D93** (2016), no. 3 031701, [arXiv:1509.01110].

[5] D. Goncalves, P. A. N. Machado, and J. M. No, *Simplified Models for Dark Matter Face their Consistent Completions*, *Phys. Rev.* **D95** (2017), no. 5 055027, [arXiv:1611.04593].

[6] J. F. Gunion and H. E. Haber, *The CP conserving two Higgs doublet model: The Approach to the decoupling limit*, *Phys. Rev.* **D67** (2003) 075019, [hep-ph/0207010].

[7] I. F. Ginzburg and I. P. Ivanov, *Tree-level unitarity constraints in the most general 2HDM*, *Phys. Rev.* **D72** (2005) 115010, [hep-ph/0508020].

[8] B. Grinstein, C. W. Murphy, and P. Uttayarat, *One-loop corrections to the perturbative unitarity bounds in the CP-conserving two-Higgs doublet model with a softly broken $\mathbb{Z}_2$ symmetry*, *JHEP* **06** (2016) 070, [arXiv:1512.04567].

[9] A. Barroso, P. M. Ferreira, I. P. Ivanov, and R. Santos, *Metastability bounds on the two Higgs doublet model*, *JHEP* **06** (2013) 045, [arXiv:1303.5098].

[10] F. Staub, *Reopen parameter regions in Two-Higgs Doublet Models*, arXiv:1705.03677.

[11] J. Alwall, R. Frederix, S. Frixione, V. Hirschi, F. Maltoni, O. Mattelaer, H. S. Shao, T. Stelzer, P. Torrielli, and M. Zaro, *The automated computation of tree-level and next-to-leading order differential cross sections, and their matching to parton shower simulations*, *JHEP* **07** (2014) 079, [arXiv:1405.0301].

[12] C. Degrande, C. Duhr, B. Fuks, D. Grellscheid, O. Mattelaer, and T. Reiter, *UFO - The Universal FeynRules Output*, *Comput. Phys. Commun.* **183** (2012) 1201–1214, [arXiv:1108.2040].

[13] **NNPDF** Collaboration, R. D. Ball et al., *Parton distributions for the LHC Run II*, *JHEP* **04** (2015) 040, [arXiv:1410.8849].

[14] **ATLAS** Collaboration, *Search for Dark Matter Produced in Association with a Higgs Boson Decaying to $b\bar{b}$ using 36 fb^{-1} of pp collisions at $\sqrt{s} = 13$ TeV with the ATLAS Detector*, *Phys. Rev. Lett.* **119** (2017), no. 18 181804, [arXiv:1707.01302].

[15] **ATLAS** Collaboration, M. Aaboud et al., *Search for an invisibly decaying Higgs boson or dark matter candidates produced in association with a Z boson in pp collisions at $\sqrt{s} = 13$ TeV with the ATLAS detector*, *Phys. Lett.* **B776** (2018) 318–337, [arXiv:1708.09624].

[16] **CMS** Collaboration, A. M. Sirunyan et al., *Search for new physics in events with a leptonically decaying Z boson and a large transverse momentum imbalance in proton-proton collisions at $\sqrt{s} = 13$ TeV*, arXiv:1711.00431.

[17] G. Cowan, K. Cranmer, E. Gross, and O. Vitells, *Asymptotic formulae for likelihood-based tests of new physics*, *Eur. Phys. J.* **C71** (2011) 1554, [arXiv:1007.1727]. [Erratum: Eur. Phys. J.C73,2501(2013)].

[18] G. Cowan, *Discovery sensitivity for a counting experiment with background uncertainty*, tech. rep., Royal Holloway, London, (2012). Available [online] http://www.pp.rhul.ac.uk/~cowan/stat/medsig/medsigNote.pdf.

[19] M. Backovic, K. Kong, and M. McCaskey, *MadDM v.1.0: Computation of Dark Matter Relic Abundance Using MadGraph5*, *Physics of the Dark Universe* **5-6** (2014) 18–28, [arXiv:1308.4955].

[20] M. Backovic, A. Martini, O. Mattelaer, K. Kong, and G. Mohlabeng, *Direct Detection of Dark Matter with MadDM v.2.0*, *Phys. Dark Univ.* **9-10** (2015) 37–50, [arXiv:1505.04190].